

ALMA MATER STUDIORUM · UNIVERSITÀ DI BOLOGNA

School of Science
Department of Physics and Astronomy
Master Degree in Physics

Real Time Data Quality Monitor and Test Beam for the SND@LHC experiment

Supervisor:
Prof. Maurizio Spurio

Submitted by:
Filippo Mei

Co-supervisor:
Dr. Gaetano Marco Dallavalle

Academic Year 2022/2023

Abstract

The use of the Large Hadron Collider as a neutrino factory was conceived about 30 years ago and it is a reality since very few years. SND@LHC is a compact, standalone experiment located in the TI18 tunnel (480 m downstream of the ATLAS interaction point) and it allows for the identification of all three flavors of neutrino interactions in the pseudorapidity region $7.2 < \eta < 8.4$ with an unexplored energy range of $100 \text{ GeV} < E < 1 \text{ TeV}$. In this work I developed a Real Time Data Quality Monitor for the SND@LHC electronic detector, allowing for an immediate evaluation of the collected data. This multi-threaded Python software was extensively used during a test beam in July-August 2023. Moreover, I describe my contribution to a preliminary analysis of the test beam data, covering muons and pions with several energies between 100 GeV and 300 GeV.

Contents

1	Neutrino Physics	5
1.1	Weak Interactions	6
1.2	Neutrino cross section	10
1.2.1	Thresholdless processes: $E_\nu \simeq 0 - 1$ MeV	10
1.2.2	Low energy nuclear processes: $E_\nu \simeq 1 - 100$ MeV	11
1.2.3	Intermediate energy processes: $E_\nu \simeq 0.1 - 20$ GeV	12
1.2.4	High energy processes: $E_\nu \simeq 20 - 500$ GeV	13
1.2.5	Uncovered energy domain: $E_\nu \simeq 0.5 - 10$ TeV	14
1.2.6	Ultra high energy neutrinos: $E_\nu \gtrsim 10$ TeV	15
1.3	Collider neutrinos	15
1.3.1	Pseudorapidity	16
1.3.2	Luminosity	17
1.4	Neutrinos beyond the Standard Model	17
1.4.1	Dirac and Majorana neutrinos	18
1.4.2	Heavy Neutral Leptons	19
1.5	Neutrino flavour oscillations	20
2	The SND@LHC Experiment	23
2.1	Physics goals	23
2.2	The SND@LHC detector	24
2.2.1	The emulsion target	24
2.2.2	The electronic detector	25
2.2.3	Readout electronics	26
2.2.4	Event reconstruction	28
2.3	Neutrino flux	29
2.3.1	Background sources	30
3	The Real Time Data Quality Monitor	35
3.1	The SND@LHC readout software	35
3.2	RTDQM Purpose and Usage	37
3.3	Software Structure	38

<i>CONTENTS</i>	3
3.4 Monitoring	40
4 Test Beam Setup and Preliminary Analysis	46
4.1 SiPM thresholds and calibration	46
4.1.1 TIA baseline and discriminators	48
4.1.2 TDC calibration	52
4.1.3 QDC calibration	52
4.2 Muons	55
4.3 Pions	60
A RTDQM main script	67

Introduction

Neutrino are elusive particles involved in several aspects of physics beyond the Standard Model. Neutrino interactions have been measured in the energy regime below 350 GeV and scarce data is present in the energy range 10 TeV - 1 PeV. The use of the Large Hadron Collider as a neutrino factory was suggested about 30 years ago with the main objective being the observation of the (at the time undiscovered) ν_τ . SND@LHC is a compact, standalone experiment located in the TI18 tunnel (480 m downstream of the ATLAS interaction point) and it allows for the identification of all three flavors of neutrino interactions in the pseudorapidity region $7.2 < \eta < 8.4$ with an unexplored energy range of $100 \text{ GeV} < 1 \text{ TeV}$. The SND@LHC detector consists of a hybrid system with a $\sim 830 \text{ kg}$ target made of tungsten plates interleaved with nuclear emulsion and electronic trackers doubling as electromagnetic calorimeter, followed by a hadronic calorimeter and a muon identification system.

In Chapter 1 the characteristics of Weak Interactions and neutrino cross section are presented, from thresholdless processes to ultra high energy neutrinos. The chapter ends with the Dirac-Majorana neutrino puzzle and its implications for the existence of Heavy Neutral Leptons.

In Chapter 2 an overview of the SND@LHC experiment goes through the physics goals, the hybrid detector (emulsion target and electronic detector) and data acquisition. In addition the neutrino flux and background sources in the SND@LHC acceptance are presented.

In Chapter 3 the Real Time Data Quality Monitor is described, from its role and integration within the SND@LHC data acquisition to the usage and available plots.

In Chapter 4 the preparation and setup for the July-August 2023 test beam are presented. Moreover, preliminary results obtained from muons and pion beams ranging in energy from 100 GeV to 300 GeV are shown.

Chapter 1

Neutrino Physics

By the early 1900s, it was already evident that the radiation emitted by radioactive materials could be categorized into only three different types, which were called α , β , and γ according to their penetration ability into matter. It was discovered that the α rays, the least penetrating, were ${}^4\text{He}$ nuclei, the γ rays, the most penetrating, were photons of high energy, and the β rays electrons. The α and γ processes are two-body decays and therefore present discrete spectra. This means that, for a given radioactive material, the energies of the α and γ rays are constant. This fact was immediately understood through conservation of energy and momentum. In fact, the value of the measured energies of the α and γ rays corresponded to the difference between the mass of the parent nucleus, the one that decays emitting radiation, and the masses of the products of the decay. In contrast, the energy spectrum of electrons measured in the β decay was continuous for each decaying element. Furthermore, calorimetric measurements showed that, on average, the electrons carried less than half of the available energy, obtained by comparing the masses of the parent and child nuclei (Figure 1.1) [1].

In 1930 Wolfgang Pauli proposed the idea of the existence of a particle with no electric charge, therefore difficult to detect, that would be emitted together with the electron, so that the sum of the energies of the two particles was constant. In 1932 Chadwick identified a neutral particle of mass comparable to that of the proton, and named it neutron. Enrico Fermi immediately realized that this was not the particle predicted by Pauli, and he differentiated the nomenclature of the two particles. He called neutron the heavy particle identified by Chadwick and neutrino the one predicted by Pauli, much lighter than the neutron. In 1934, Fermi developed the decay theory which predicted the emission of an electron and of an (anti)neutrino due to a nuclear interaction different from that which keeps protons and neutrons bound in nuclei, the Weak Interaction (WI). In 1956, Frederick Reines and Clyde Cowan observed for the first time antineutrinos [2], which were produced by a nuclear reactor and detected through the inverse β decay reaction (Figure 1.2)



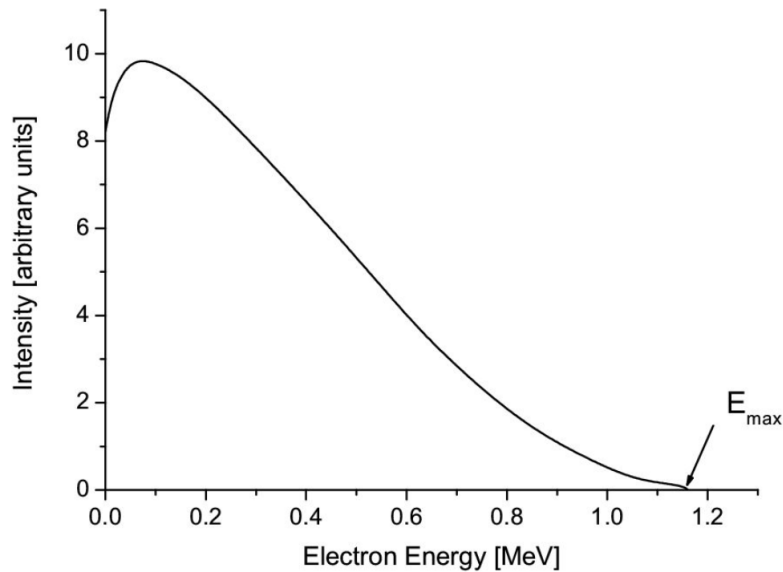


Figure 1.1: A typical β decay spectrum. The energy of the electron is not discrete, but continuous. The reason is the presence of another particle in the final state, the neutrino.

In the mid-1950s, the study of the WI highlighted that parity is not conserved in processes induced by this interaction. The consequences of this fact on the characteristics of neutrinos are relevant. In all the observed processes, the direction of the neutrino spin is contrary to that of their motion, and the opposite is true for antineutrinos. The idea that there were different types of neutrinos was already established when, in 1962, the muon-type neutrino was identified. In 1975, a new lepton was discovered, the τ , of mass 1777 MeV, much heavier than the electron and muon. It was then hypothesized that this lepton was also associated with another neutrino, which was identified in 2001. The vector bosons mediating the weak interaction, W^\pm and Z^0 , were identified in 1983 at the proton-antiproton collider at CERN in Geneva. Since the early 1990s, there has been extensive experimental activity directed to the study of neutrino properties.

1.1 Weak Interactions

The current description of phenomena induced by WI is based on the exchange of the W^\pm and Z^0 bosons [1]. In this framework, the study of the interaction is related to the knowledge of the strength and the manner in which the two bosons couple with quarks and leptons.

The optimal measure for evaluating the strength of the WI is that of the decay of

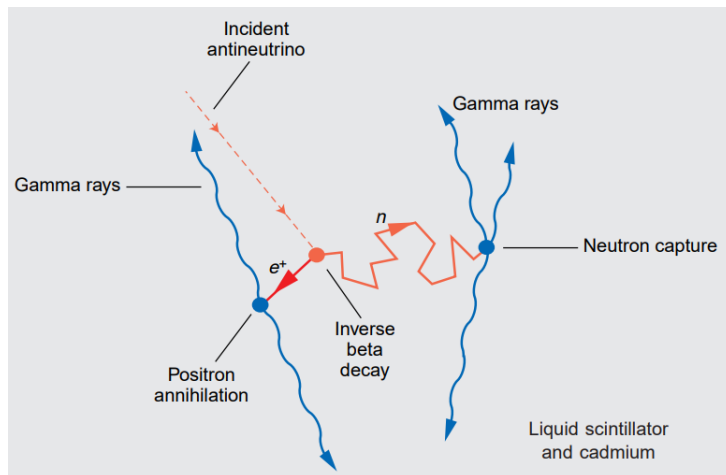


Figure 1.2: Raines and Cowan’s idea to detect neutrinos. The positron produced in the inverse β decay quickly finds an electron and produces two γ rays by pair-annihilation, a very distinctive event in which the two 0.5 MeV photons are detected simultaneously in opposite directions. In the meantime, the neutron wanders about until it is captured by a cadmium nucleus. The resulting nucleus releases about 9 MeV of energy in gamma rays that will again cause the liquid scintillator to produce a tiny flash of visible light. This sequence of two flashes of light separated by a few microseconds is the double signature of inverse β decay and confirms the presence of a neutrino [3].

the muon

$$\mu^- \longrightarrow e^- + \bar{\nu}_e + \nu_\mu \quad (1.2)$$

represented by the diagram in Figure 1.3. Indeed, it is a process that involves only leptons, thus not affected by the presence of other interactions, such as the Strong one in the case of the neutron decay. The contribution to the transition amplitude of the term describing the transition of W from one point to another in the diagram is given by the expression [4]

$$\mathcal{A} \propto g \frac{1}{q^2 - \omega^2 + M_W^2} g, \quad (1.3)$$

where q is the magnitude of the momentum transferred from the muon to the decay products and ω is the transferred energy, given by the difference between electron and muon masses (the neutrinos involved in the process are considered massless). The term M_W represents the mass of the W and is about 80 GeV. The term g is a real number that represents the strength with which the W couples to the other particles. This number is commonly referred to as the coupling constant. Given that, as in this case, $q^2 - \omega^2 \ll M_W^2$ for many of the processes studied, the Equation 1.3 is simplified by

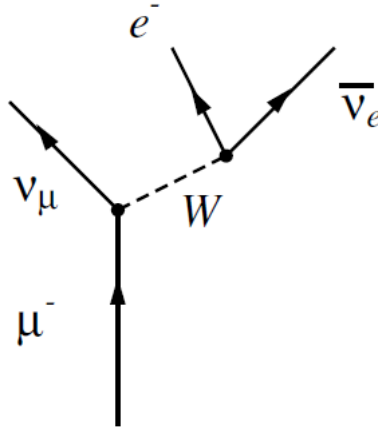


Figure 1.3: Feynman diagram of the muon decay.

neglecting the momentum and the transferred energy

$$g \frac{1}{q^2 - \omega^2 + M_W^2} g \simeq \frac{g^2}{M_W^2} = \frac{\sqrt{2}}{\pi} \frac{1}{(\hbar c)^2} G_F \quad (1.4)$$

where a new coupling constant G_F was defined, known as Fermi's. From experimental data it is obtained

$$\frac{G_F}{(\hbar c)^3} = 1.166 \times 10^{-5} \text{ GeV}^{-2}. \quad (1.5)$$

To grasp the quantitative meaning of this value it is useful to consider the charged current process

$$\nu_\mu + e^- \longrightarrow \mu^- + \nu_e \quad (1.6)$$

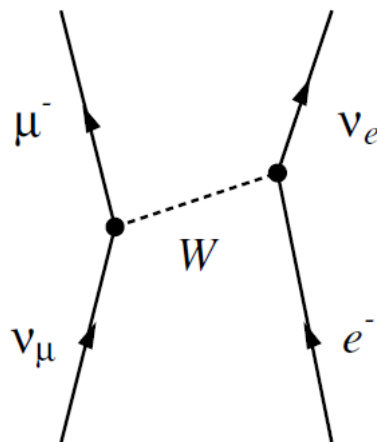
shown in Figure 1.4. For neutrino energies $E_{\nu_\mu} \ll M_W$, the expression of the cross section for this process is given by [1]

$$\sigma = \frac{G_F^2}{\pi(\hbar c)^4} 2m_e c^2 E_{\nu_\mu} \simeq 10^{-45} E_{\nu_\mu} \text{ m}^2, \quad (1.7)$$

where m_e is the mass of the electron and E_{ν_μ} is in GeV. The extremely small value of this cross section can be better appreciated by computing the free average neutrino path length in matter. Considering a neutrino with energy of 1 MeV propagating in iron, whose number of electron per m^3 is $\rho = 2.2 \times 10^{30} \text{ m}^{-3}$, the average path length is

$$L = \frac{1}{\rho\sigma} \simeq 3.74 \times 10^{17} \text{ m} \simeq 40 \text{ light years}. \quad (1.8)$$

These numbers give an idea of the elusiveness of neutrinos and the difficulty in detecting them.

Figure 1.4: Feynman diagram of a charged current process for a ν_μ .

Once the magnitude of the WI coupling is understood, it is left to examine the coupling modes between leptons and W^\pm and Z^0 bosons. The discovery of parity violation in 1957 by Madame Wu implied a combination of two types of interaction with opposite parities. In principle, up to five different types of operator in the WI matrix element are allowed by relativistic invariance. These operators are named according to their transformation properties under spatial reflection: vector (V), axial vector (A), scalar (S), pseudoscalar (P) and tensor (T). Experimental results showed that leptons and antileptons involved in weak decays have opposite longitudinal polarisations, i.e. opposite helicities (projection of the velocity over the spin, Figure 1.5), and this narrowed the choice of operators down to the V and A operators. A general combination of V and A amplitudes would correspond to an operator of the form [4]

$$\mathcal{O} = V + \alpha A \quad (1.9)$$

The fact that massless fermions are produced in pure helicity eigenstates $H = -1$, requires $\alpha = -1$. Hence, the WI is a $V - A$ theory with maximal parity violation.

The quantity that is conserved in the processes induced by the WI is not helicity but a slightly different quantity called chirality, which, in contrast to helicity, remains constant regardless of the reference system in which it is observed (relativistic invariant). Therefore, due to the $V - A$ coupling, only particles that have chirality -1 (called left-handed), and the antiparticles with chirality $+1$ (called right-handed) are sensitive to the WI. For massless particles chirality and helicity coincide. In the case of massive particles, chirality is conserved in WI, and can be described as a linear combination of the two helicity states. For massive particles the left-handed chirality is described by the negative helicity component plus a positive helicity component with a contribution greater the larger the mass of the particle. The opposite holds for antiparticles.

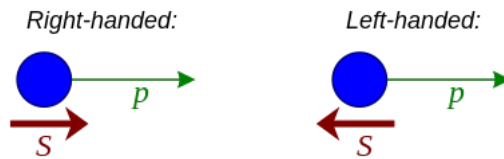


Figure 1.5: Helicity indicates whether the spin of a fermion points along (positive helicity) or against (negative helicity) the direction of travel. Chirality indicates whether a particle is left handed or right handed. The connection between the two is that, at the speed of light, left handed particles have negative helicity, and right handed particles have positive helicity. Left-handed and right-handed particles travelling below light speed each have a precise mixture of helicities, depending on their mass.

1.2 Neutrino cross section

An understanding of neutrino cross sections is a truly essential element of any experimental neutrino program. The known reactions of neutrinos with matter fall completely within the purview of the Standard Model of particle physics. However, one quickly finds that theoretical approximations which work well in one particular energy regime completely break down elsewhere (Figure 1.6).

The full description of the interaction is encoded within the matrix element [6]. The Standard Model readily provides a prescription to describe neutrino interactions via the leptonic charged current and neutral current in the WI Lagrangian. These interactions all fall within the context of the general gauge theory of $SU(2)_L \times U(1)_Y$. This readily divides the types of possible interactions for neutrinos into two broad categories: a charged current (CC) exchange and a neutral current (NC) exchange. The former is mediated by the exchange of a charged W^\pm boson. The latter describes the exchange of the neutral boson, Z_0 (Figure 1.7). So far, experiments in laboratory have been conducted with neutrino energies up to a few hundred GeV. SND@LHC is for the first time exploring the energy range up to a few TeV, making a bridge to measurements with neutrinos from astrophysical sources. In the next sections, neutrino interactions will be described across various energy scales.

1.2.1 Thresholdless processes: $E_\nu \simeq 0 - 1$ MeV

Such processes include:

- coherent scattering, which involves the NC exchange where a neutrino interacts coherently with the nucleus

$$\nu + A_N^Z \longrightarrow \nu + A_N^{*Z}. \quad (1.10)$$

At low energies the cross section should be coherent across all the nucleons present in the nucleus. As a result, the cross section grows as the square of the atomic

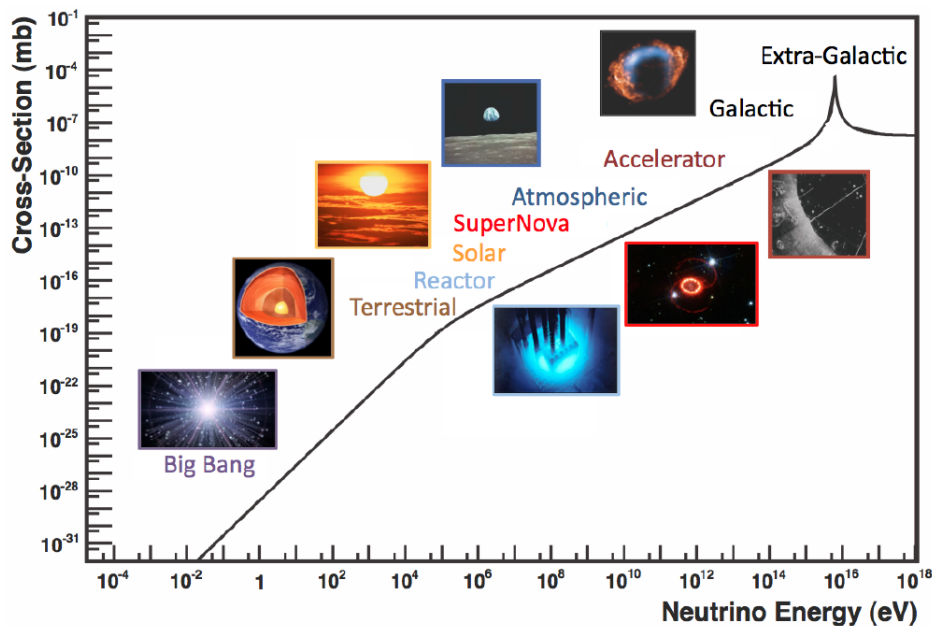


Figure 1.6: Representative example of various neutrino sources across decades of energy. The electroweak cross-section for $\bar{\nu}_e + e^- \rightarrow \bar{\nu}_e + e^-$ scattering on free electrons as a function of neutrino energy (for a massless neutrino) is shown for comparison. The peak at 10^{16} eV is due to the W resonance [5].

number A^2 . Despite the strong coherent enhancement enjoyed by this particular process, this interaction has yet to be detected experimentally. Part of the obstacle stems from the extremely small energies of the recoil. The interaction has also been proposed as a possible mechanism for detecting cosmic relic neutrinos.

- neutrino capture on radioactive nuclei, sometimes referred as enhanced or stimulated β decay due to the same observable final states



This mechanism too remains to be observed.

1.2.2 Low energy nuclear processes: $E_\nu \simeq 1 - 100$ MeV

As the energy of the neutrino increases, it is possible to probe the target nucleus at smaller and smaller length scales. Whereas coherent scattering only allows to resolve the nucleus as a single coherent structure, higher energies allow to access nucleons individually. Unlike the thresholdless scattering mechanisms discussed previously, these low energy nuclear processes have been studied extensively in neutrino experiments. The

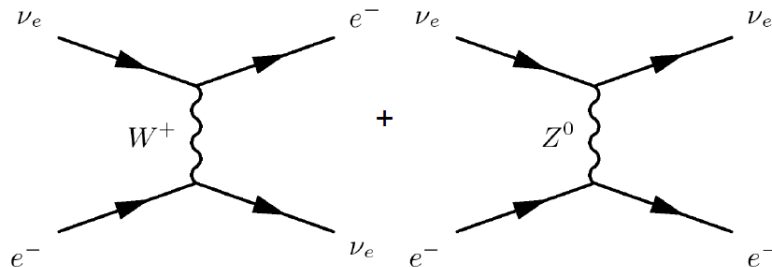


Figure 1.7: Feynman tree-level diagram for charged (on the left) and neutral (on the right) current components of $\nu_e + e^- \rightarrow \nu_e + e^-$ scattering.

simplest nuclear interaction that we can study is antineutrino-proton scattering, otherwise known as inverse beta decay:

$$\bar{\nu}_e + p \rightarrow e^+ + n. \quad (1.12)$$

This reaction is typically measured using neutrinos produced from fission in nuclear reactors. The WI governs both the processes of decay as well as scattering amplitudes.

1.2.3 Intermediate energy processes: $E_\nu \simeq 0.1 - 20 \text{ GeV}$

Moving up further in energy, the description of neutrino scattering becomes increasingly more diverse and complicated. At these intermediate energies, several distinct neutrino scattering mechanisms start to play a role. The possibilities fall into three main categories [5]:

- elastic and quasi-elastic scattering. Neutrinos can elastically scatter off an entire nucleon liberating a nucleon (or multiple nucleons) from the target. In the case of CC neutrino scattering, this process is referred to as quasi-elastic (QE) scattering, whereas for NC scattering this is traditionally referred to as elastic scattering. For neutrino energies less than 2 GeV, neutrino-hadron interactions are predominantly QE. In a QE interaction, the neutrino scatters off an entire nucleon rather than its constituent parton:

$$\nu_l + n \rightarrow l^- + p, \quad \bar{\nu}_l + p \rightarrow l^+ + n. \quad (1.13)$$

Whereas in NC scattering:

$$\nu + n \rightarrow \nu + n, \quad \nu + p \rightarrow \nu + p, \quad \bar{\nu} + n \rightarrow \bar{\nu} + n, \quad \bar{\nu} + p \rightarrow \bar{\nu} + p. \quad (1.14)$$

- resonance production (RES). Neutrinos can excite the target nucleon to a resonance state. The resultant baryonic resonance (Δ , N^*) decays to a variety of possible mesonic final states producing combinations of nucleons and mesons.

- deep inelastic scattering (DIS). Given enough energy, the neutrino can resolve the individual quark constituents of the nucleon. This reaction manifests in the creation of a hadronic shower and of the charged lepton in the case of a CC interaction.

Neutrino and antineutrino CC cross sections measurements across this energy range (Figure 1.8) approach a linear dependence on neutrino energy. Due to lower statistics and higher background, $\bar{\nu}$ cross sections and both cross sections at lower energy have larger uncertainties. Looking at specific neutrino flavours, the CC cross section for ν_τ is severely altered because of the larger τ mass (which translates into larger threshold energy) with respect to the other leptons (Figure 1.9).

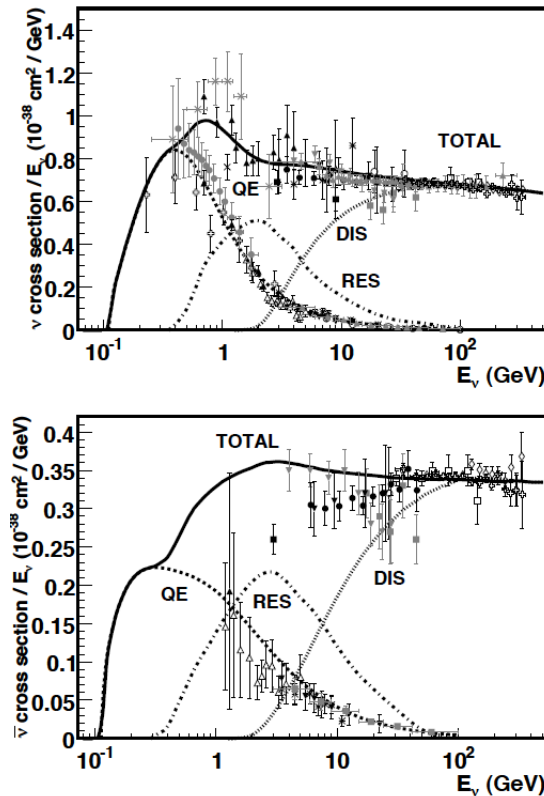


Figure 1.8: Total neutrino (upper plot) and antineutrino (lower plot) per nucleon CC cross sections divided by neutrino energy and plotted as a function of the neutrino energy [7].

1.2.4 High energy processes: $E_\nu \simeq 20 - 500$ GeV

The most common high energy interaction is deep inelastic scattering, in which the neutrino can scatter off an individual quark inside the nucleon via the exchange of a

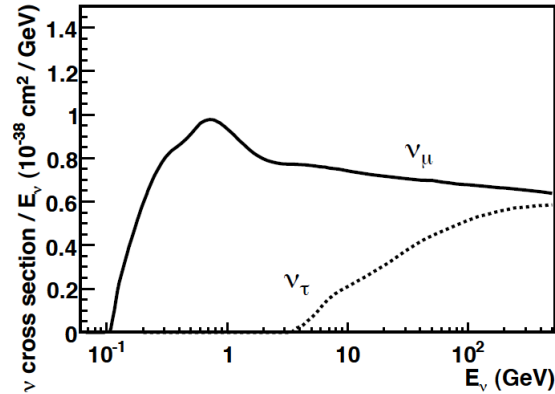


Figure 1.9: Total charged current per nucleon cross sections for ν_μ (solid) and ν_τ (dashed) divided by neutrino, plotted as a function of neutrino energy [5].

virtual W^\pm or Z^0 boson producing a lepton and a hadronic system in the final state (Figure 1.10). Both CC and NC processes are possible:

$$\nu_l + N \longrightarrow l^- + X, \quad \bar{\nu}_l + N \longrightarrow l^+ + X, \quad \nu_l + N \longrightarrow \nu_l + X, \quad \bar{\nu}_l + N \longrightarrow \bar{\nu}_l + X. \quad (1.15)$$

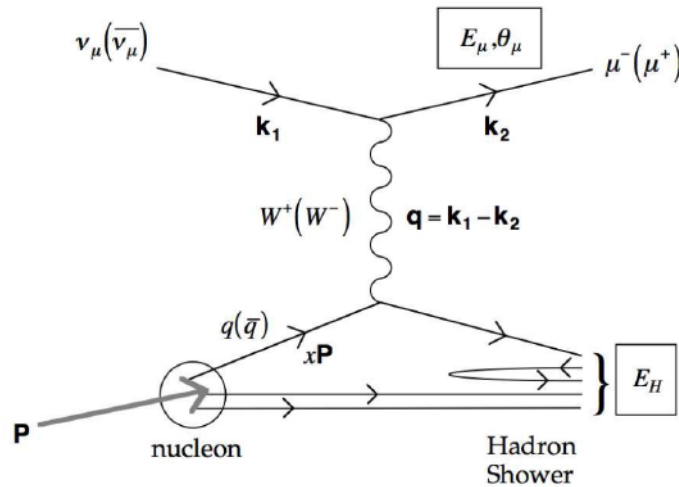


Figure 1.10: First-order Feynman diagram for CC deep inelastic neutrino scattering [8].

1.2.5 Uncovered energy domain: $E_\nu \simeq 0.5 - 10$ TeV

This energy range is a transition region between high energy neutrinos and the astrophysical ultra high energy neutrinos (Figure 1.11). Currently, it is being explored for the first time by the SND@LHC experiment [9].

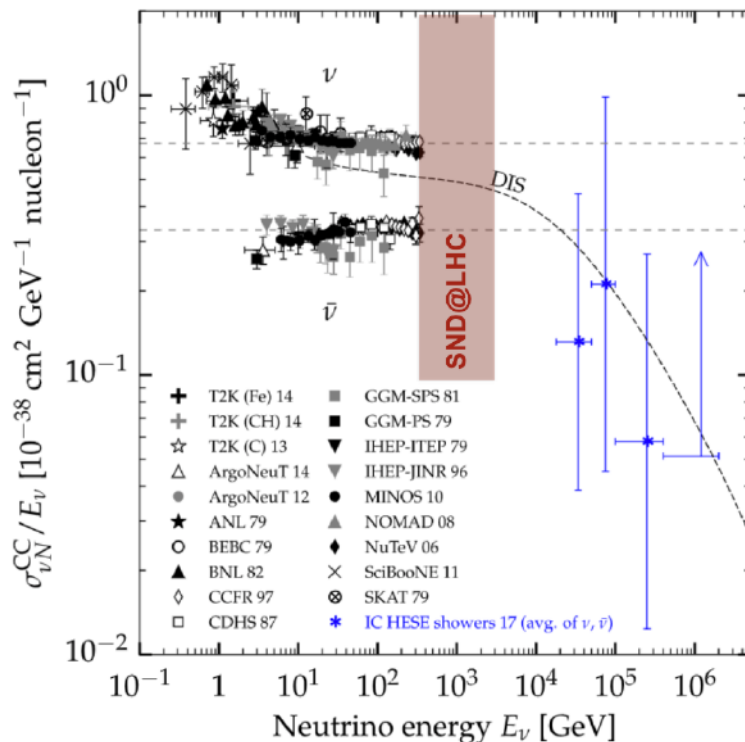


Figure 1.11: Charged-current neutrino-nucleon cross section measurements [10]. The thick dashed curve is a standard prediction of DIS cross section. The SND@LHC experiment is currently exploring the \sim TeV uncovered energy domain.

1.2.6 Ultra high energy neutrinos: $E_\nu \gtrsim 10$ TeV

Data about neutrinos at this extreme energy scale is quite scarce. A variety of astrophysical objects and mechanisms become accessible at these energies, providing information that is complementary to that already obtained from electromagnetic or hadronic observations. Neutrino-electron scattering is usually sub-dominant to any neutrino-nucleus interaction because of its small target mass. However, there is one notable exception when the neutrino undergoes a resonant enhancement from the formation of an intermediate W boson in $\bar{\nu}_e + e^-$ interactions [11]. This resonance formation takes place at $E_{res} = M_W^2/2m_e = 6.3$ PeV and it is the most prominent neutrino interaction up to 10^{21} eV (Figure 1.12).

1.3 Collider neutrinos

Neutrinos can be produced as secondary particles by hadron interaction. On Earth, high-energy neutrinos can be produced only by proton accelerators. Usually, secondary

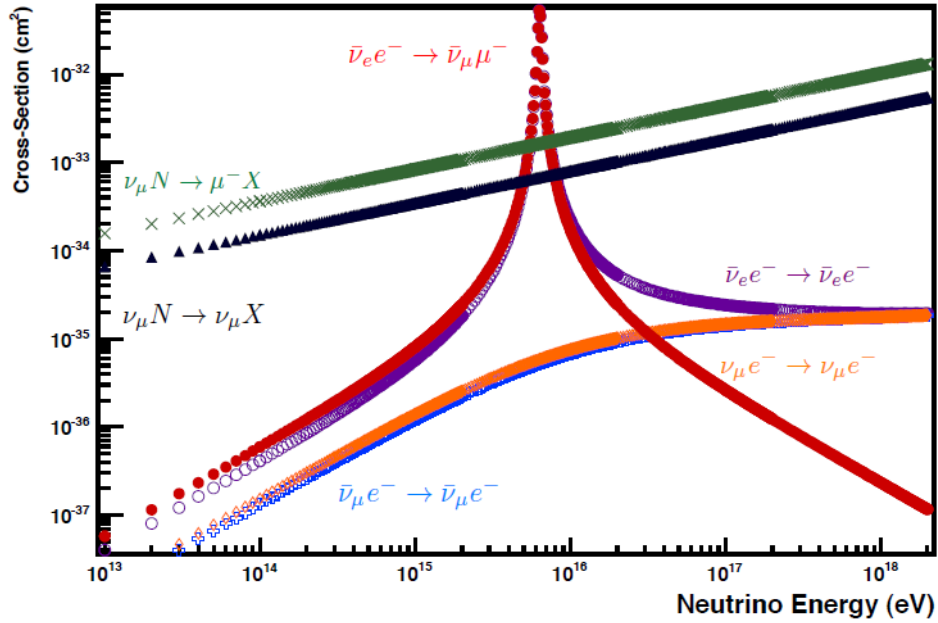


Figure 1.12: Neutrino electron and nucleon scattering in the ultra high energy regime. The leptonic W resonance channel is clearly evident (red filled circles and violet hollow circles) [5].

neutrinos are produced in beam-dump experiments, where accelerated protons (or nuclei) interact with target material at rest. So far, the maximum neutrino energies reached in this way are well below 1 TeV.

The use of the Large Hadron Collider (LHC) as a neutrino factory was suggested about 30 years ago with the main objective being the observation of the (at the time undiscovered) ν_τ . The passive use of proton-proton interactions in a collider to produce secondary neutrinos is an absolute novelty. Two fundamental quantities characterizing collider neutrinos are pseudorapidity and luminosity.

1.3.1 Pseudorapidity

Pseudorapidity is a concept used in particle physics to describe the angular distribution of particles produced in high-energy collisions, particularly in particle accelerators like the LHC at CERN. In this context, where particles are produced in all directions, the rapidity and pseudorapidity variables provide a more convenient way to describe particle angles with respect to spherical coordinates. The Rapidity of a particle is defined as

$$y = \frac{1}{2} \ln \left(\frac{E + p_z}{E - p_z} \right), \quad (1.16)$$

where E is the energy of the particle and p_z is the component of the particle's momentum along the beam axis. The difference between the rapidities of two particles is invariant with respect to Lorentz boosts along the z -axis. This is the key reason why rapidities are so crucial in accelerator physics. Pseudorapidity is a simpler approximation of rapidity which works well in the high-energy limit. It's defined as:

$$\eta = -\ln\left(\tan\frac{\theta}{2}\right), \quad (1.17)$$

where θ is the polar angle of the particle with respect to the beam axis.

1.3.2 Luminosity

Luminosity is a crucial parameter that quantifies the intensity of particle collisions and has a direct impact on the number of events and the precision of measurements in high-energy physics experiments. Luminosity has units of inverse area per unit time and it is defined as the ratio of the number of events detected dN in a certain period of time dt to the cross-section σ :

$$L = \frac{1}{\sigma} \frac{dN}{dt}. \quad (1.18)$$

A related quantity is the integrated luminosity:

$$L_{\text{int}} = \int L dt. \quad (1.19)$$

The luminosity and integrated luminosity are useful values to characterize the performance of a particle accelerator. In particular, all collider experiments aim to maximize their integrated luminosity, as the higher the integrated luminosity, the more data is available to analyze for a given process.

1.4 Neutrinos beyond the Standard Model

Ever since the proposal by Pauli, the mass of neutrinos has been the topic of intense experimental and theoretical investigation. At the time of the Pauli proposal, the neutrino mass was postulated to be of the order of the electron mass or even massless. Today, there is evidence for neutrino masses, although only two small values of squared-mass differences are known. The origin of the small neutrino mass is still a mystery. It is commonly believed that neutrino masses are a low-energy manifestation of physics beyond the Standard Model and their smallness is due to a suppression generated by a new high-energy scale, perhaps related to the unification of forces. This is achieved, for example, with the see-saw mechanism [12].

1.4.1 Dirac and Majorana neutrinos

A Dirac neutrino mass can be generated with the same Higgs mechanism that gives masses to quarks and charged leptons in the Standard Model [4]. The only extension of the SM that is needed is the introduction of right-handed components of the neutrino fields. Such a model is sometimes called the minimally extended Standard Model, in which the asymmetry in the SM between the lepton and quark sectors due to the absence of right-handed neutrino fields is eliminated. Let us recall, however, that the right-handed neutrino fields are fundamentally different from the other elementary fermion fields because they do not participate in WI (as well as Strong and Electromagnetic Interactions, as all neutrino fields). Thus, their only interaction is gravitational. For this reason, they are called sterile. On the other hand, the normal left-handed neutrino fields that participate in WI are usually called active. The number of active neutrino flavours can be obtained from the decay width of the Z^0 boson, and the result is three [13]. However, the number of sterile right-handed neutrino fields is not constrained by the theory.

Exploiting the Higgs mechanism, the neutrino masses m_k would be [4]:

$$m_k = \frac{y_k^\nu v}{\sqrt{2}} \quad (k = 1, 2, 3) \quad (1.20)$$

where y_k^ν are real and positive Yukawa couplings and v is the Higgs vacuum expectation value. These neutrino masses that we have obtained with this mechanism are proportional to v , as the masses of charged leptons and quarks. However, it is known that the masses of neutrinos are much smaller than those of charged leptons and quarks. Still, there is no explanation of the very small values of the y_k^ν that are needed. As for the other leptons, the conserved current related to the lepton number implies that neutrinos have $L = +1$, whereas antineutrinos have $L = -1$. Therefore, the lepton quantum numbers are different for neutrinos and antineutrinos (charged leptons and antileptons are also distinguished by the lepton number, but they are distinguished by the electric charge as well). Hence, the Dirac nature of massive neutrinos would imply that neutrinos and antineutrinos are different particles.

The Dirac equation for a chiral fermion field $\psi = \psi_L + \psi_R$ is equivalent to the equations

$$i\gamma^\mu \partial_\mu \psi_L = m\psi_R \quad (1.21)$$

$$i\gamma^\mu \partial_\mu \psi_R = m\psi_L \quad (1.22)$$

which are coupled by the mass m of the fermion. If the fermion is massless (as the SM neutrinos), it can be described by a single chiral field (ψ_L or ψ_R), which has only two independent components. Actually, even a massive fermion can be described with only

a two-components spinor (instead of four) with the assumption that ψ_L and ψ_R are not independent [14]. Ettore Majorana found that the two fields should be related in the following way:

$$\psi_R = \xi \mathcal{C} \bar{\psi}_L^T, \quad (1.23)$$

where \mathcal{C} is the charge conjugation matrix and ξ is a phase factor. Applying this relation to the Eq. 1.21 and 1.22 it follows that

$$\psi_L^C = \mathcal{C} \bar{\psi}_L^T, \quad (1.24)$$

where ψ_L^C is the charge conjugate field. Thus, the Majorana field can be written as

$$\psi = \psi_L + \psi_L^C = \psi^C, \quad (1.25)$$

which implies the equality of particle and antiparticle (only neutral fermions can be described by a Majorana field). Among known elementary fermions only the neutrinos are neutral and they can be Majorana particles. The Dirac and Majorana descriptions of a neutrino have different phenomenological consequences only if the neutrino is massive. If the neutrino is massless, since the left-handed chiral component of the neutrino field obeys Eq. 1.21 in both the Dirac and Majorana descriptions and the right-handed chiral component is irrelevant for neutrino interactions, the Dirac and Majorana theories are physically equivalent.

From these considerations, it is clear that in practice one can distinguish a Dirac from a Majorana neutrino only by measuring some effect due to the neutrino mass. Moreover, the mass effect must not be of kinematical nature, because the kinematical effects of Dirac and Majorana masses are the same (for example in neutrino oscillations). One way to find if neutrinos are Majorana particles is the search for neutrinoless double β -decay.

1.4.2 Heavy Neutral Leptons

The smallness of neutrino masses can be explained by the so-called “seesaw” mechanism [15], which postulates the existence of a number of electroweak-singlet (sterile) neutrino interaction eigenstates. However, this mechanism does not specify the number of electroweak-singlet neutrinos. Massive neutrinos with a mass $m_N \gg \text{eV}$ are called “Heavy Neutral Leptons” (HNL).

A model that incorporates the seesaw mechanism is the neutrino Minimal Standard Model (νMSM) [16]. In this model, three right-handed HNLs are added to the SM. A lighter neutrino N_1 is expected to have a mass in the keV scale, the two heavier neutrinos N_2, N_3 are expected to have a mass in the GeV scale [17]. Thus, N_2, N_3 can be produced at LHC through intermediate decay of hadrons produced in proton-proton collision. Then they can decay into SM particles (Figure 1.13). SND@LHC is expected to provide measurements for the direct search of HNLs [18].

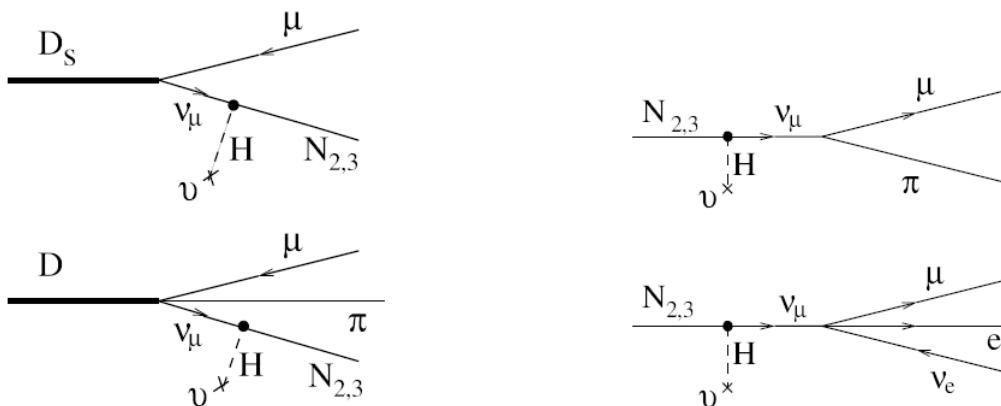


Figure 1.13: Possible HNL production via an intermediate hadronic state (on the left) and subsequent decay in SM particles (on the right). The predicted mass range of HNLs allowed for production at LHC and SND@LHC can provide measurements.

1.5 Neutrino flavour oscillations

Neutrino oscillation is a quantum mechanical phenomenon proposed in the late 1950s by Bruno Pontecorvo [19]. The oscillations are generated by the interference of different massive neutrinos, which are produced and detected coherently because of their very small mass differences. Neutrinos produced in CC WI in association with a charged lepton are weak-eigenstates: ν_e , ν_μ or ν_τ . In general these weak-eigenstates do not have a well defined mass, and can be written as linear superposition of three mass-eigenstates ν_1 , ν_2 and ν_3 [4]. In general we can write

$$|\nu_\alpha\rangle = \sum_j U_{\alpha j}^* |\nu_j\rangle, \quad (1.26)$$

with $\alpha = e, \mu, \tau$, $j = 1, 2, 3$ and U is the Pontecorvo-Maki-Nakagawa-Sakata (PMNS) unitary mixing matrix. In the case of three neutrino flavors, the mixing matrix can be parameterized with three mixing angles θ_{12} , θ_{13} , θ_{23} and one CP violating phase δ :

$$U = \begin{pmatrix} 1 & 0 & 0 \\ 0 & c_{23} & s_{23} \\ 0 & -s_{23} & c_{23} \end{pmatrix} \begin{pmatrix} c_{13} & 0 & s_{13}e^{-i\delta} \\ 0 & 1 & 0 \\ -s_{13}e^{-i\delta} & 0 & c_{13} \end{pmatrix} \begin{pmatrix} c_{12} & s_{12} & 0 \\ -s_{12} & c_{12} & 0 \\ 0 & 0 & 1 \end{pmatrix} \quad (1.27)$$

where $c_{jk} = \cos \theta_{jk}$, $s_{jk} = \sin \theta_{jk}$. Neutrinos are produced in weak-eigenstates, propagate in mass-eigenstates and finally detected in weak-eigenstates. Since the time evolution of each mass-eigenstate produces different phases, it is shown that the probability amplitude of finding a neutrino produced as $|\nu_\alpha\rangle$, after some time t in a flavor state $|\nu_\beta\rangle$ is

$$P(\nu_\alpha \longrightarrow \nu_\beta, t) = \sum_{k,j} U_{\alpha k}^* U_{\beta k} U_{\alpha j} U_{\beta j}^* e^{-i(E_k - E_j)t} \quad (1.28)$$

which is periodical in time. For ultra-relativistic neutrinos holds

$$E_k - E_j \simeq \frac{m_k^2 - m_j^2}{2E} = \frac{\Delta m_{kj}^2}{2E}. \quad (1.29)$$

Moreover in neutrino oscillation experiments, the propagation time t is not measured. What is known is the distance L ($\simeq ct$) between the source and the detector. Considering the simple case of two-neutrino mixing, with all of the above approximations, the transition probability reduces to

$$P(\nu_\alpha \rightarrow \nu_\beta, t) = \sin^2 2\theta \sin^2 \left(1.27 \Delta m^2 [\text{eV}^2] \frac{L[\text{km}]}{E[\text{GeV}]} \right). \quad (1.30)$$

An important characteristic of neutrino oscillations is that the transitions to different flavors cannot be measured if

$$\frac{\Delta m^2 L}{2E} \ll 1, \quad (1.31)$$

as the transition probability would be almost zero. On the other hand, if

$$\frac{\Delta m^2 L}{2E} \gg 1 \quad (1.32)$$

only the average transition probability is observable, due to the smearing coming from experimental errors, yielding information only on $\sin^2 2\theta$ (Figure 1.14). Neutrino experiments choose the appropriate value of L/E to maximize the sensitivity with respect to a specific Δm^2 (fixed by nature), given by

$$\frac{\Delta m^2 L}{2E} \simeq 1. \quad (1.33)$$

Currently, considering three neutrino families, it is estimated that $\Delta m_{21} \sim 10^{-5} \text{ eV}^2$ and $\Delta m_{31} \sim 10^{-3} \text{ eV}^2$. In SND@LHC, neutrinos are detected ~ 480 away from their production point and their energy is $\sim 1 \text{ TeV}$. Thus, the $L/E \sim 1/2000$ ratio does not allow flavor oscillations.

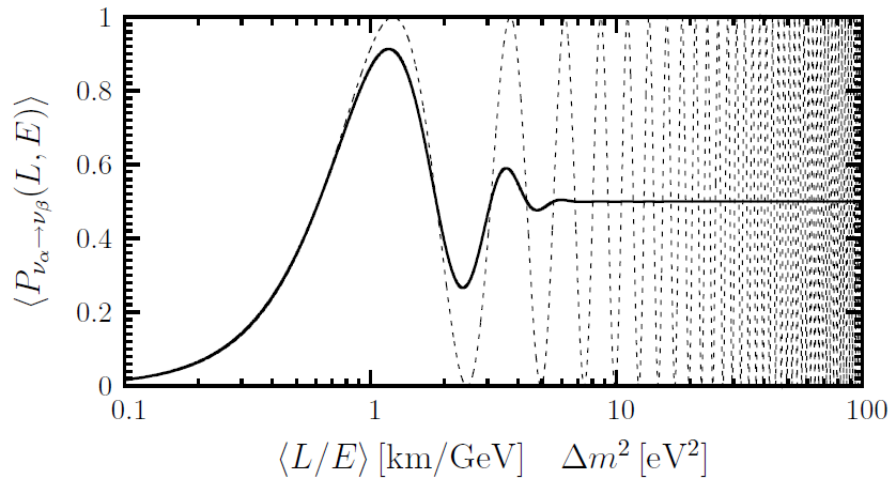


Figure 1.14: Averaged transition probability (solid line) over a Gaussian L/E distribution as a function of $\langle L/E \rangle$ and unaveraged probability (dotted line), assuming $\sin^2 2\theta = 1$ [4].

Chapter 2

The SND@LHC Experiment

Proton-proton collisions at LHC will produce a high intensity beam of $O(10^{12})$ neutrinos in the far forward direction with energies up to a few TeV. SND@LHC is a compact, standalone experiment located in the TI18 tunnel, 480 m downstream of the ATLAS Interaction Point (IP) that allows for the identification of all three flavors of neutrino interactions in the pseudorapidity region $7.2 < \eta < 8.4$ [9]. The SND@LHC detector consists of a hybrid system with a ~ 830 kg target made of tungsten plates interleaved with nuclear emulsion and electronic trackers, followed by a hadronic calorimeter and a muon identification system.

2.1 Physics goals

The main physics goals of the SND@LHC experiment are summarised in the following list:

- The neutrino-nucleon cross section region between 350 GeV and 10 TeV is currently unexplored. As seen above, neutrinos produced in $p - p$ collisions within the SND@LHC pseudorapidity acceptance, cover this energy range.
- Electron neutrinos can be used as a probe of the production of charmed hadrons [20]. Furthermore, the measurement of the charmed hadrons can be translated into a measurement of the corresponding open charm production in the same rapidity window, given the linear correlation between the parent charm quark and the hadron. The dominant partonic process for associated charm production at the LHC is the scattering of two gluons producing a $c\bar{c}$ pair [21]. The average lowest momentum fraction of interacting gluons probed by SND@LHC is $\sim 10^{-6}$. The extraction of the gluon parton distribution function at such low values of x , where it is completely unknown, could provide constraints and lowering the uncertainty of QCD predictions, particularly relevant for experiments at future hadron colliders.

- Since the three neutrino flavours can be identified, the lepton flavour universality can be tested in the neutrino sector by measuring the ratio of ν_e/ν_τ and ν_e/ν_μ interactions.
- Direct search of feebly-interacting particles (FIPs) such as dark scalars, Heavy Neutral Leptons and dark photons [22]. It will be possible to disentangle the scattering of massive FIPs and neutrinos, with a significance that depends on the mass of the particle.

2.2 The SND@LHC detector

The SND@LHC apparatus is composed of a target region preceded by a veto system and followed downstream by a hadronic calorimeter and muon identification system (Figure 2.1). The target region, with a mass of about 830 kg, is instrumented with five walls of Emulsion Cloud Chambers (ECC), each followed by a Scintillating Fibre (SciFi) plane [9]. The ECC technology alternates emulsion films, acting as tracking devices with micrometric accuracy, with passive material (Tungsten) acting as the neutrino target. The SciFi planes provide the timestamp for the reconstructed events and have an appropriate time resolution for time-of-flight measurements. The combination of the emulsion target and the target tracker also acts as an electromagnetic calorimeter, with a total of 85 radiation lengths X_0 and 1.5 interaction lengths λ_{int} . Veto, emulsion target and target tracker are contained in a 30% borated polyethylene and acrylic box which has the dual function of acting as a neutron shield from low energy neutrons and maintaining controlled temperature and humidity levels in order to guarantee optimal conditions for emulsion films. The hadronic calorimeter and muon identification system are located downstream of the target and consist of eight 20 cm-thick iron slabs corresponding to 9.5 interaction lengths λ_{int} in total, each followed by one or two planes of 1 cm-thick scintillating bars.

2.2.1 The emulsion target

The emulsion target is made of five walls with a sensitive transverse size of 384×384 mm² [9]. Each wall consists of four bricks as illustrated in Figure 2.2. Each brick is made of 60 emulsion films with a transverse size of 192×192 mm², interleaved with 59 1 mm-thick tungsten plates. Tungsten was selected as target material in order to maximise the interaction rate per unit volume. Moreover, the low intrinsic radioactivity makes tungsten a suitable material for an emulsion detector. The reconstruction of track segments in consecutive films provide the vertex reconstruction with an accuracy at the micron level. A nuclear emulsion film has two 70 μ m-thick sensitive layers on both sides of a 170 μ m-thick transparent plastic base. The passage of a charged particle leaves

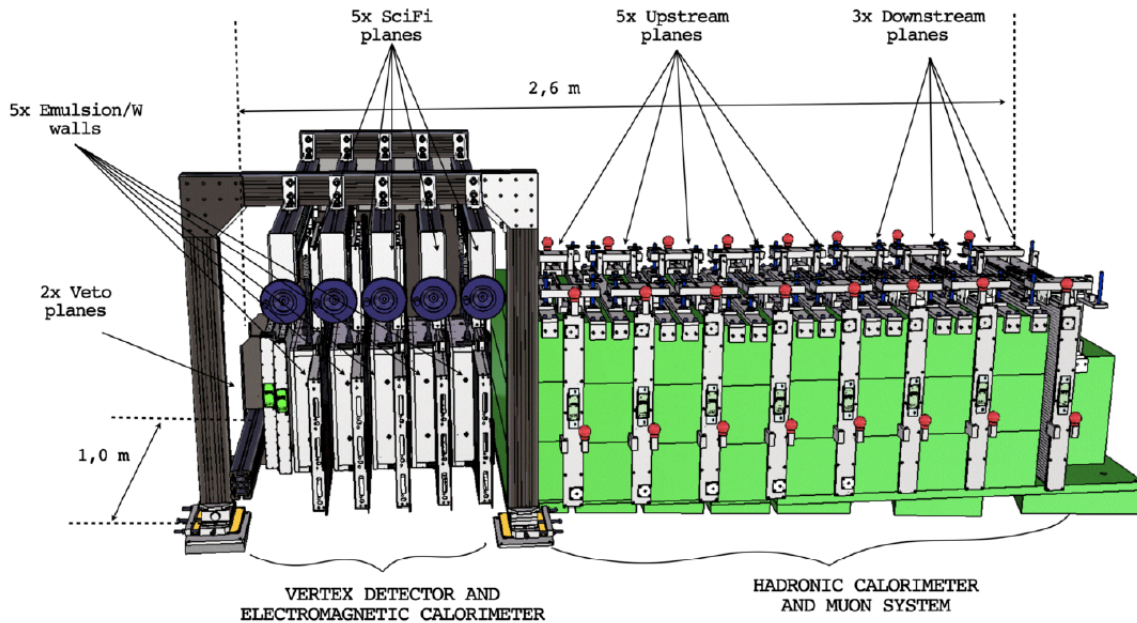


Figure 2.1: The layout of the SND@LHC apparatus: two veto planes followed by a target region and an hadronic calorimeter and muon system [9].

trails of hits on both sensitive layers, providing two track segments. By connecting the two segments, the slope of the track can be measured with milliradian accuracy. The emulsion target is replaced every $\sim 20 \text{ fb}^{-1}$ in order to avoid an unmanageable amount of combinatorics during track reconstruction. Then, emulsion films are developed and analysed by fully automated optical microscopes.

2.2.2 The electronic detector

The most upstream component of the electronic detector is the veto system. The veto system aims at rejecting charged particles entering the detector acceptance, mostly muons coming from the ATLAS IP. It is located upstream of the target region and comprises two parallel planes of seven $1 \times 6 \times 42 \text{ cm}^3$ stacked scintillating bars read out on both ends by Silicon Photomultipliers (SiPMs). Bars are wrapped in aluminized Mylar foil to ensure opacity and isolate them from light in adjacent bars.

Following the veto system, the next component of the electronic detector is SciFi. The role of SciFi trackers is two-fold: assign a timestamp to neutrino interactions reconstructed in the ECC walls and provide an energy measurement of electromagnetic showers. Moreover, the combination of SciFi and scintillating bars of the muon detector will also act as a non-homogeneous hadronic calorimeter for the measurement of the energy of the hadronic jet produced in the neutrino interaction. Each SciFi station consists

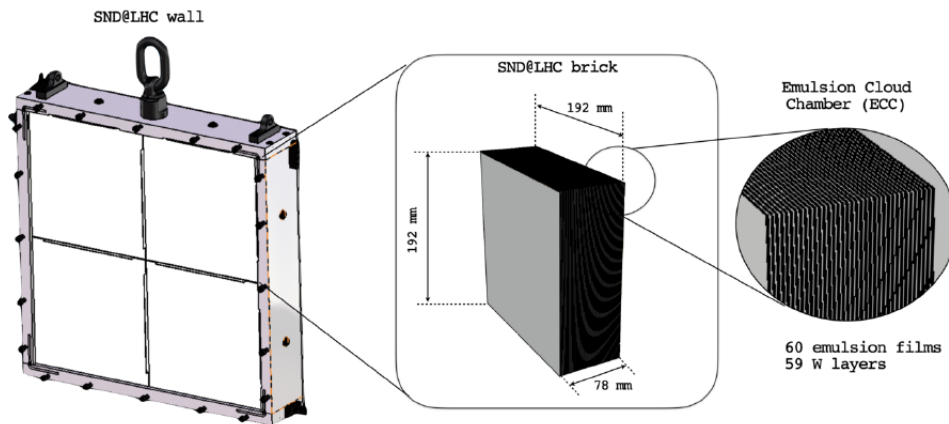


Figure 2.2: An emulsion wall is composed of four bricks, each consisting of 60 emulsion films interleaved with 59 tungsten sheets [9].

of two $40 \times 40 \text{ cm}^2$ planes, alternating X and Y orientated mats. Each mat comprises six densely packed staggered layers of $250 \mu\text{m}$ diameter polystyrene-based scintillating fibres read out by SiPM arrays. The single particle spatial resolution in one view is $\sim 150 \mu\text{m}$ and the time resolution for a particle crossing both X and Y mats of one plane is $\sim 250 \text{ ps}$ [23].

The last module of the electronic detector is the muon system and hadronic calorimeter, which consists of two parts: UpStream (US), the first five stations, and DownStream (DS), the last three stations. Each US station consists of 10 stacked horizontal scintillator bars of $1 \times 6 \times 82.5 \text{ cm}^3$, similar to the veto detector, resulting in a coarse Y view (Figure 2.3). Every US bar end is viewed by eight SiPMs: six “large” ($6 \times 6 \text{ mm}^2$, $50 \mu\text{m}$ pitch) ones and two “small” ($3 \times 3 \text{ mm}^2$, $10 \mu\text{m}$ pitch) ones [9]. A DS station consists of two layers of thinner $1 \times 1 \times 82.5 \text{ cm}^3$ bars arranged in alternating X and Y directions, allowing for a spatial resolution along each axis of less than 1 cm. Every horizontal DS bar end is viewed by one “small” SiPM, the vertical ones are viewed only from one side. The time resolution for a single DS detector bar is $\sim 120 \text{ ps}$. The eight scintillator planes are interleaved with 20 cm thick iron blocks. Both US and DS bars are covered in aluminized Mylar foil to ensure opacity. The finer spatial resolution of the DS detector allows for the identification of muon tracks exiting the detector.

2.2.3 Readout electronics

Every sub-system of the electronic detector is read out with the same data acquisition (DAQ) electronics, consisting of front-end (FE) boards, and DAQ readout boards [9]. They read out the signals from the SiPMs, digitize them and send the recorded data to a DAQ server. The system runs synchronously with the LHC bunch crossing clock,

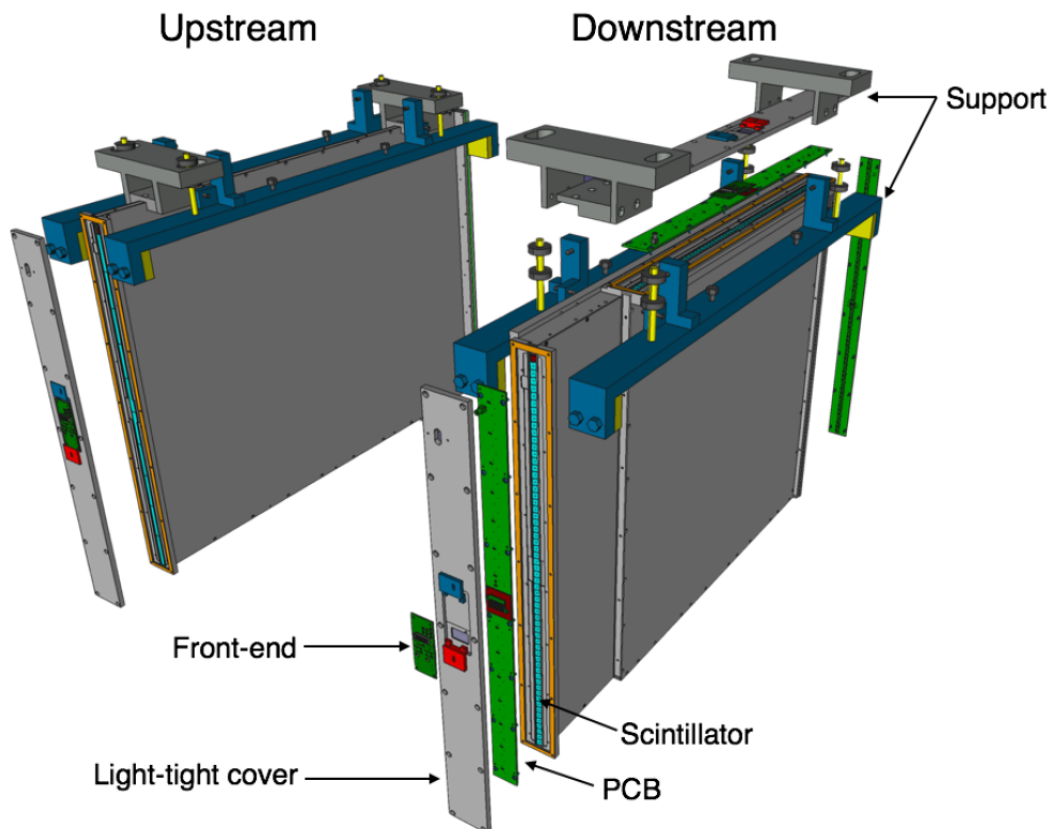


Figure 2.3: Illustration of a DS and an US station of the muon system and hadronic calorimeter [9]. A DS station is made of two planes with bars oriented along the X and Y axis.

and operates in a trigger-less mode (all hits recorded by each board are transmitted to the DAQ server). Noise reduction is performed at the front-end level by setting an appropriate threshold for each channel, and on the DAQ server after event building.

The front-end (FE) boards (Figure 2.4) are based on the TOFPET2 ASIC by PET-sys. The TOFPET2 is a 64-channels readout and digitization ASIC which incorporates signal amplification circuitry, discriminators, charge integrators, charge-to-digital converters (QDC) and time-to-digital converters (TDC). A combination of up to three discriminators with configurable thresholds can be used.

The DAQ readout boards (Figure 2.5) feature an Altera Cyclone V FPGA. Each DAQ board is equipped with four high-speed connectors for the FE boards, an optical fibre receiver to receive the clock and synchronous signals from the TTC system and a 1 Gb Ethernet port used for data and command transmission.

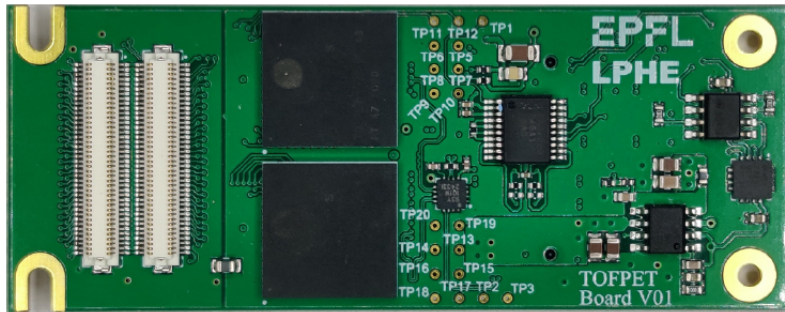


Figure 2.4: Photo of the FE board. The two TOFPET2 ASICs (centre) and the SiPM connectors (left) are visible.



Figure 2.5: Photo of the DAQ board. The four FE board connectors are visible on the left, the TTCrx and optical receiver on the bottom-right.

2.2.4 Event reconstruction

The identification of the neutrino flavour is done in charged current interactions by identifying the charged lepton produced at the primary vertex (Figure 2.6). Electrons will be clearly separated from neutral pions thanks to the micrometric accuracy and fine sampling of the Emulsion Cloud Chambers, which will enable photon conversions downstream of the neutrino interaction vertex to be identified. Muons will be identified by the presence of a track penetrating the whole muon system. Tau leptons will be identified topologically in the ECCs, through the observation of the tau decay. FIPs will be identified through their scattering off electrons and nuclei of the emulsion target material. In the case of a FIP elastic scattering off atomic electrons, the experimental signature consists of an isolated recoil electron that can be identified through the development of

an electromagnetic shower in the target region. For FIPs interacting elastically with a proton, instead, an isolated proton will produce a hadronic shower in the detector.

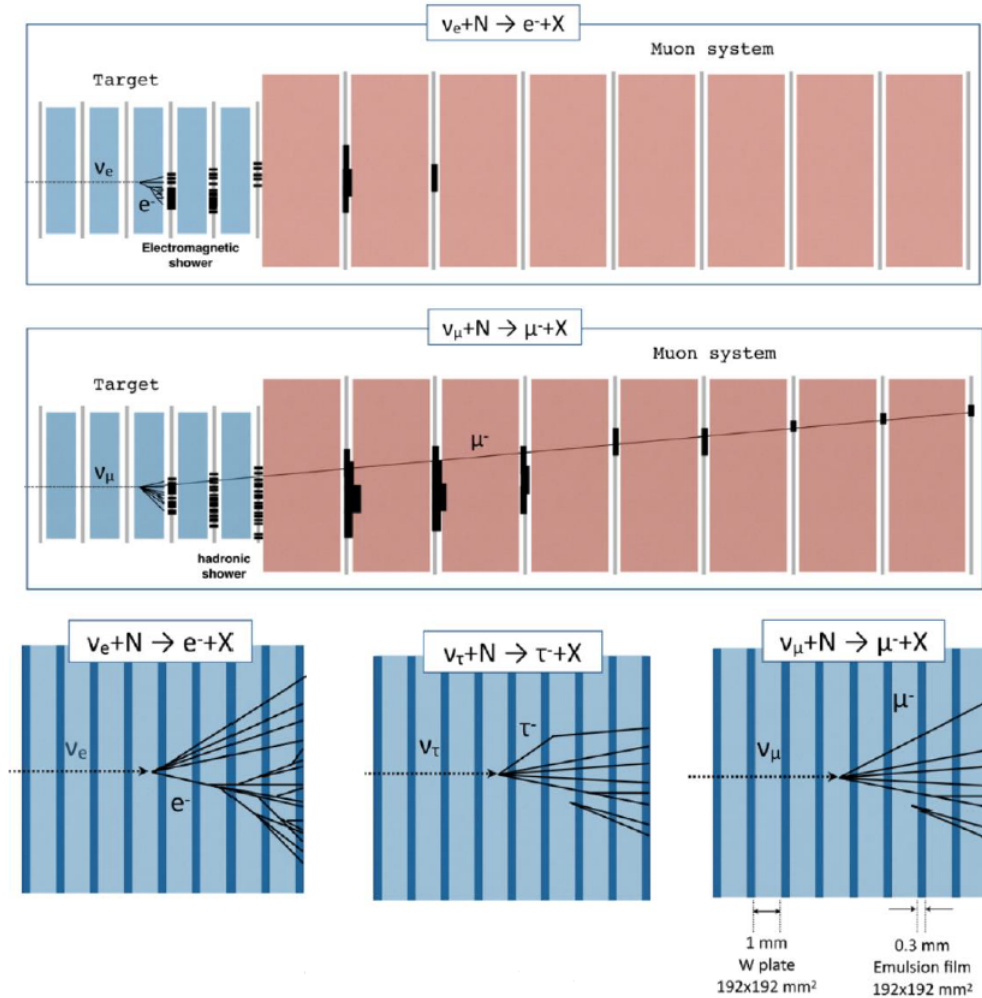


Figure 2.6: Examples of event signatures for different neutrino flavours, identified through the lepton produced in the primary vertex. ν_μ will produce a muon detected by the muon system, ν_τ will present a tau decay in the ECCs.

2.3 Neutrino flux

Neutrinos in $p - p$ interactions in the ATLAS IP arise promptly from leptonic W and Z decays, and b and c quark decays. They are subsequently also produced in the decays of pions and kaons [24]. Simulations show the flux of the different neutrino and anti-neutrino types in the (η, E_ν) plane [25] (Figure 2.7). The majority of ν_e and ν_μ

originated from the decay of charmed hadrons, with around 10% of ν_e interactions within the acceptance arising from K decay, particularly K^0 s with energies below 200 GeV. The contribution of beauty hadron decays was estimated to be approximately 3%, using the the PYTHIA8 event generator [26]. On the other hand, the distributions of ν_μ and $\bar{\nu}_\mu$ were significantly influenced by a softer component resulting from π and K decays, particularly at low energy, which explains the differing intensity scales in Figure 2.7. The average energies within the acceptance region also differed, with muon neutrinos having an average energy of around 150 GeV, while electron and tau neutrinos had an average energy of approximately 400 GeV. Concerning the ν_τ , the momentum on ν_τ produced in the chain

$$D_s \rightarrow \tau \nu_\tau \rightarrow X^- \tau \nu_\tau \quad (2.1)$$

led to a correlation between η_ν and E_ν which can be clearly seen in the bottom panel. In the case of ν_τ , there was no contribution at low energy. Moreover Figure 2.8 shows the energy spectrum of the different types of incoming neutrinos and anti-neutrinos, in the SND@LHC acceptance, as predicted by simulations. Thus, neutrinos in the energy range $0.1 < E_\nu < 1$ TeV are expected.

The high intensity of $p-p$ collisions achieved by the LHC turns into a large expected neutrino flux in the forward direction, and the high neutrino energies imply relatively large neutrino cross-sections, resulting in significant physics potential even for a detector with a relatively modest size. GENIE is used to simulate neutrino interactions with the SND@LHC detector material. During LHC Run 3 (2022-2023), with an expected integrated luminosity of 250 fb^{-1} , about 1700 CC and 550 NC neutrino interactions are expected in the tungsten target, from muon neutrinos (72%) electron neutrinos (23%) and tau neutrinos (5%).

2.3.1 Background sources

Machine-induced backgrounds decrease rapidly with increasing distance from the interaction point and away from the beam line [25]. Muons reaching the detector location are the main source of background for the neutrino search. They can either enter the target without being detected by the veto system and generate showers via bremsstrahlung or deep inelastic scattering, or interact in the surrounding material and produce neutral particles that can then mimic neutrino interactions in the target [23]. The estimate of the penetrating muon background is based on the expected flux in the fiducial volume and on the inefficiency of detector planes used as veto. The expected muon flux in the fiducial area is $1.69 \times 10^4 \text{ cm}^{-2}/\text{fb}^{-1}$. The measured rate in the same area during the 2022 run validated the Monte Carlo simulation [27]. The overall veto system inefficiency, estimated with reconstructed muon tracks during the 2022 run, amounts to 5.3×10^{-12} , thus making the background induced by muons entering the fiducial volume (Figure 2.9) negligible. Neutral particles (mainly neutrons and K_L^0 's) originating from primary muons

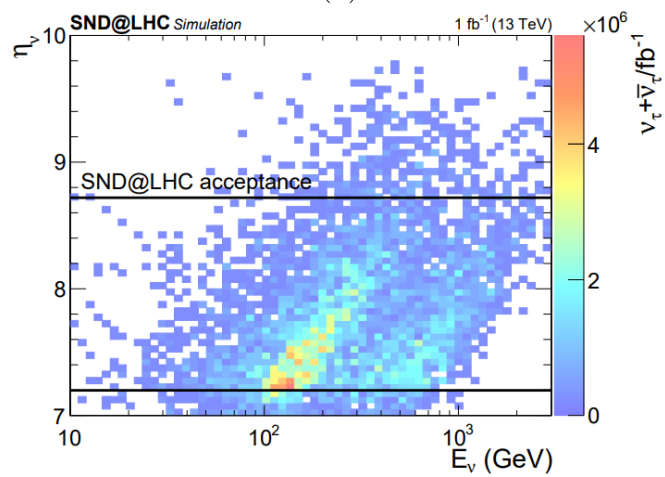
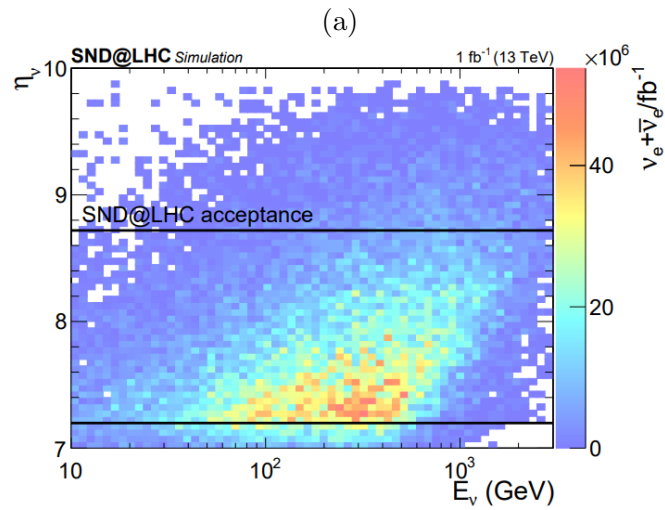
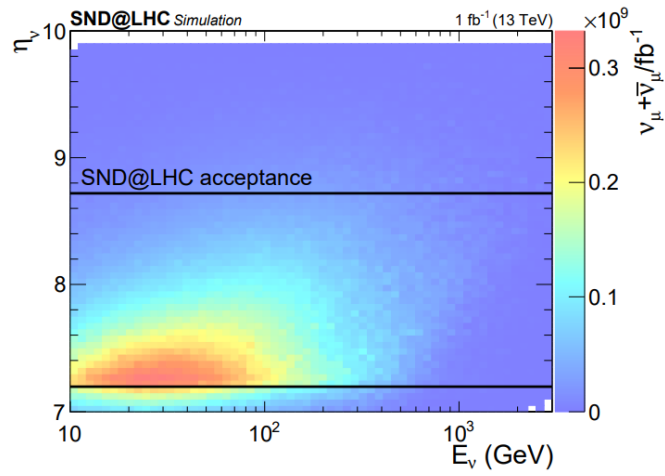


Figure 2.7: Neutrino and anti-neutrino flux as a function of energy E_ν and pseudo-rapidity η_ν for muon (a), electron (b) and tau (c) neutrinos [24].

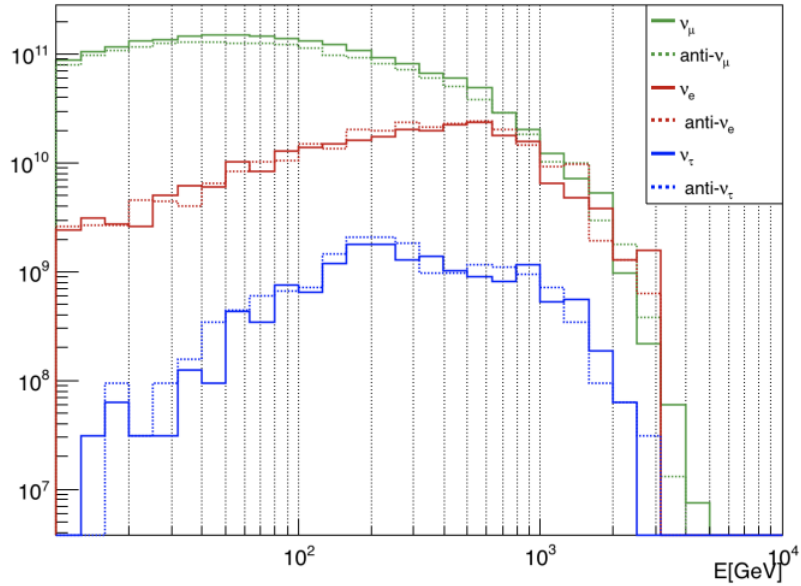


Figure 2.8: Energy spectrum of the different types of incoming neutrinos and anti-neutrinos as predicted by simulations, normalized to 150 fb^{-1} [24].

interacting in rock and concrete in front of the detector can potentially mimic a neutrino interaction since they do not leave any incoming trace in the electronic detectors, and can create a shower in the target. Still, they are mainly rejected by the veto system due to accompanying charged particles originating from the primary muon interaction. This is shown with simulations of the energy spectrum of such neutral hadrons entering the fiducial volume (Figure 2.10).

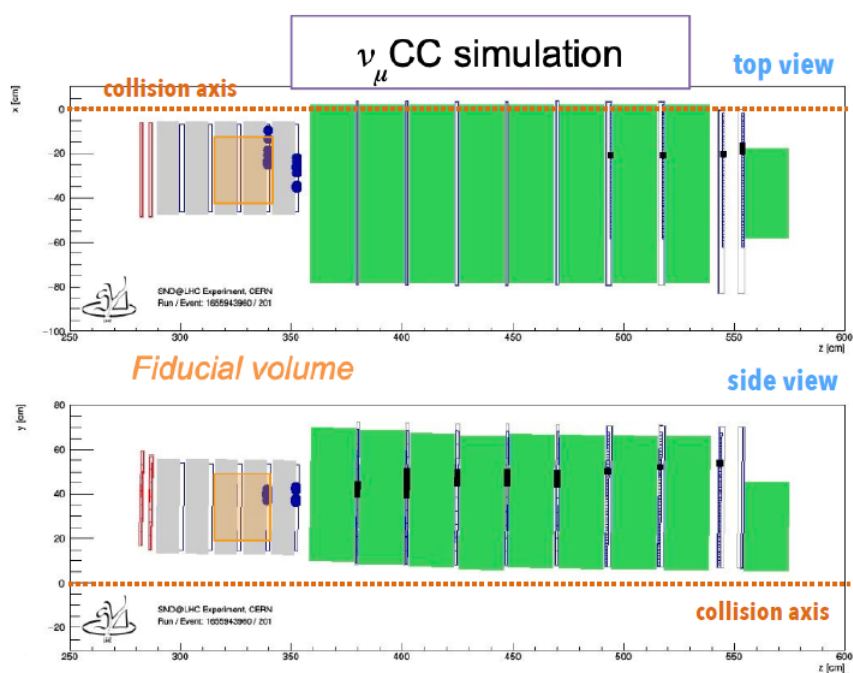


Figure 2.9: Current fiducial volume selected for ν_{μ} event reconstruction [23]. Only interactions in the third and fourth tungsten walls are considered, providing excellent background rejection.

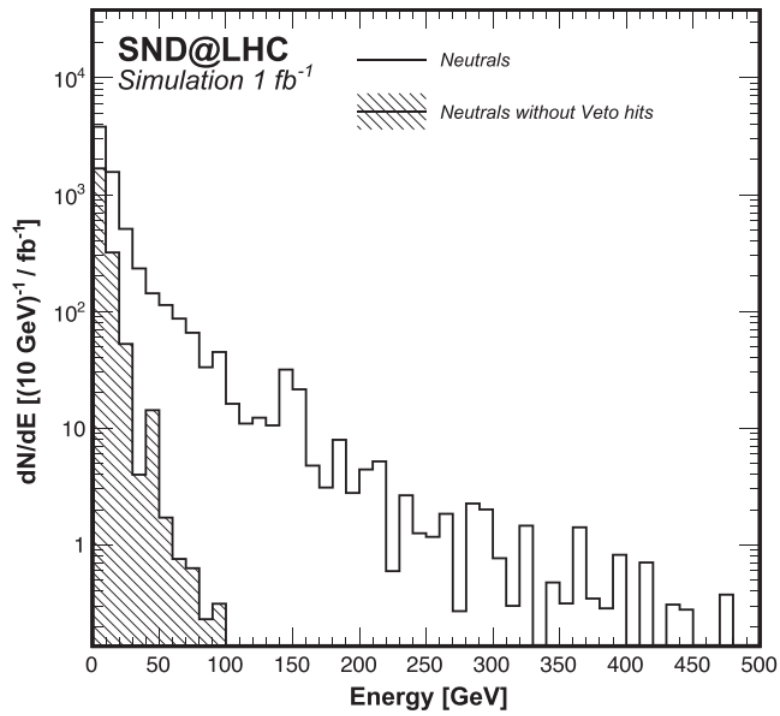


Figure 2.10: Simulated energy spectrum of neutral hadrons produced by muon interactions in the rock and concrete entering the SND@LHC acceptance. The shaded area shows the spectrum after rejecting events with hits in the veto system due to accompanying charged particles [23].

Chapter 3

The Real Time Data Quality Monitor

The Real Time Data Quality Monitor (RTDQM) that I developed for this thesis work is a multi-threaded Python software, integrated as a subsystem of the SND@LHC Experiment Control System (ECS) [9], which controls data acquisition. The RTDQM takes data from the DAQ server as soon as it is written by the DAQ system (every 30 seconds or when the data buffer is full), then performs quality checks, detector performance checks, and a first analysis on the collected data. The structure is modular by design, allowing to choose the desired information to be displayed. When a data taking run begins, the ECS starts the RTDQM, which is able to run independently. Every plot produced by the RTDQM is displayed locally on the PC that runs the software and on a web page (updating in real-time). The whole source code is public on GitHub (https://github.com/FelixofRivia/SNDatLHC_RTDM).

3.1 The SND@LHC readout software

Each DAQ board transmits all the recorded hits to the DAQ computer server, where event building is performed. The hits are grouped into events based on their timestamp, and saved to disk as a ROOT file. The readout process is fully controlled by the ECS, from starting servers to starting the data taking, sending periodic triggers, monitoring the status of each element. The ECS (Figure 3.1) is the top-level control of the experiment online system, providing a unified framework to control the hardware and software. The ECS is a layer above the other online systems, preserving their autonomy to operate independently. With this architecture, the various online components do not strictly require the ECS to operate. The ECS also performs the logging of the relevant detector information. The ECS is designed to operate the online system automatically, controlled by a global finite state machine that receives the status of the LHC and of the detector

to perform predefined actions in order to run the data taking and recover from errors. The LHC clock (40.079 MHz bunch crossing frequency) and orbit clock (11.245 kHz revolution frequency of the LHC) signals are obtained from the LHC Beam Synchronous Timing (BST) system via optical fibres. Variations of several nanoseconds in the phase of the clock are to be expected due to temperature changes. For this reason, the absolute timing offset is calibrated with the timestamps of the muons generated by proton-proton collisions at the ATLAS IP and detected in SND@LHC.



Figure 3.1: The ECS Graphical User Interface. The ECS is the top-level software of the SND@LHC online system, providing a unified framework for the control of hardware and software.

The event building process is structured in two main steps, shown in Figure 3.2. In the first step, hits collected by all boards and belonging to the same event, i.e. with time stamps within 25 ns, are grouped into “events”. The choice of this time window is related to the time interval between bunch crossings in LHC. The event timestamp corresponds to the timestamp of the earliest hit within the event. The events are then filtered and processed online, before being written to disk. The noise filter used in SND@LHC during 2023 requires hits in at least 4 SciFi planes, 2 US planes and 3 DS planes. The DAQ server writes the recorded data to a local disk. At the end of each run the data are transferred to a permanent storage.

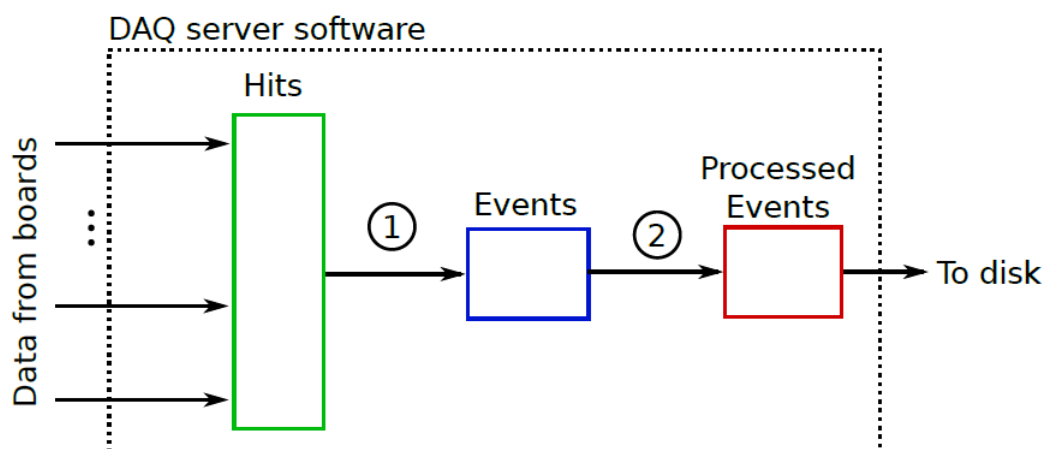


Figure 3.2: Schematic view of the event builder process. First, the collected hits are grouped into events. Then, the events are filtered and written to disk.

3.2 RTDQM Purpose and Usage

The purpose of the RTDQM is an immediate evaluation of the collected data of the electronic detector of SND@LHC. This makes it possible to take prompt action in case of errors or malfunctions and to point out issues to be fixed during the offline analysis. Moreover, stable and detailed information on the electronic detector allows to optimize the replacement timing of the emulsion target, which should collect an integrated luminosity not exceeding 20 fb^{-1} . The RTDQM is designed to be a user-friendly tool, in fact, all that is required is to select from a CSV file the desired graphs. Additionally, the desired plots can be selected through the dedicated ECS page (Figure 3.3). The software was widely used both during the 2023 test beam and is used throughout Run 3.

This software is meant to be used on ROOT files written by the SND@LHC data acquisition program. Each file is a partition of a Run and contains a ROOT tree with up to 10^6 events. Once the Run number is selected, the program will try to read through all the corresponding partitions. The RTDQM can be called using

```
user@host $ python3 monitor.py --runNumber --fileNumber --beamMode
```

Where:

- runNumber is an integer representing the desired run number;
- fileNumber is the desired starting file (partition) within a run (the first one is 0);
- beamMode is a string describing the status of the beam, used to select the most appropriate plotting parameters.

To stop the program, enter `Ctrl+\`

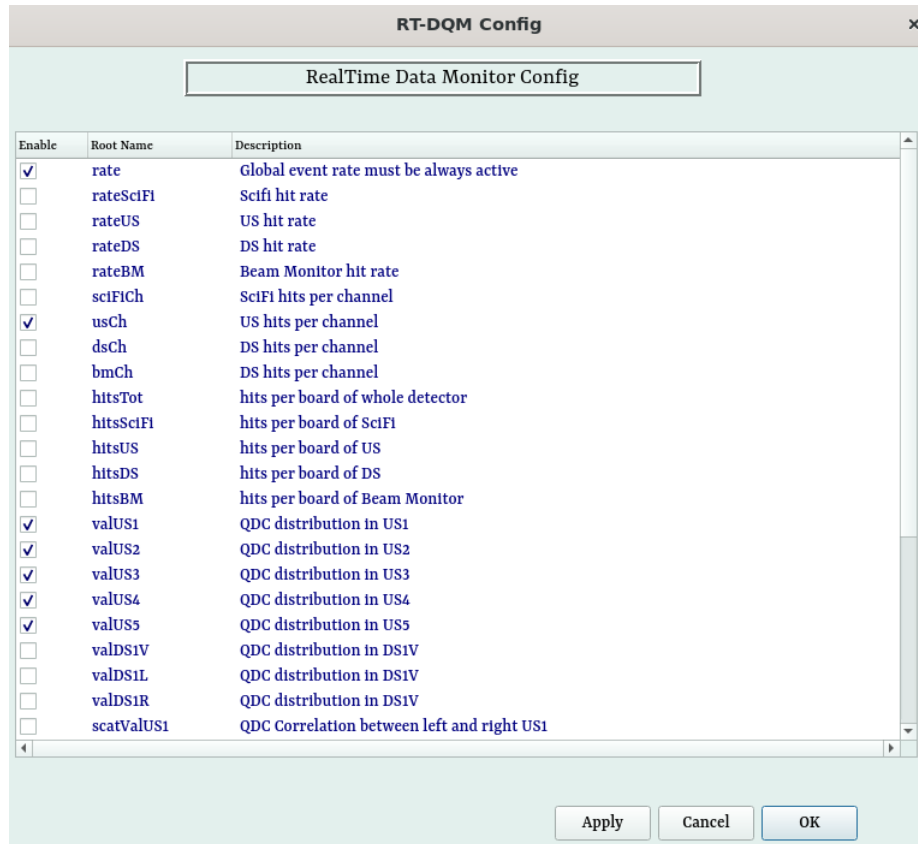


Figure 3.3: Graphical User Interface for the RTDQM plot selection via the SND@LHC ECS.

3.3 Software Structure

This software is developed in a Python 3.8 environment, using the modules `ROOT`, `numpy`, `argparse`, `threading`, `os`, `time`, `json`, `math` and `pydim`. The RTDQM main script initializes variables, reads the list of desired plots from a CSV file and creates a thread for each (Figure 3.4). The software is divided in the following way:

- `monitor.py`: the main script which initializes all parameters and creates threads;
- `board_mapping.json`: configuration file for the DAQ boards mapping to detector subsystems;
- `plot_config.csv`: configuration file for the selection of the desired monitoring plots;
- `luminosity.py`: script plotting the luminosity of ATLAS provided by `pydim` in real time (feature not available outside CERN network);

- `task.py`: script with utility functions used by threads;
- `header.py`: file with global variables shared by threads;
- `reader.py`: script which loads the desired file with data from the event tree and loops through the events. Whenever the code runs out of events, it tries to update the file and (if more events are present) resumes where it left off. This allows the code to read an active file;
- `ratePlots.py`: file with functions used to plot event/hit rate;
- `hitPlots.py`: file with functions used to plot histograms with hits per plane/board;
- `hitMaps.py`: file with functions used to plot the 2D (XY) spread of the hits in a detector plane;
- `timeAlign.py`: file with functions used to visualize the time alignment between boards;
- `valuePlots.py`: file with functions used to plot the QDC value measured by SiPMs in each station.

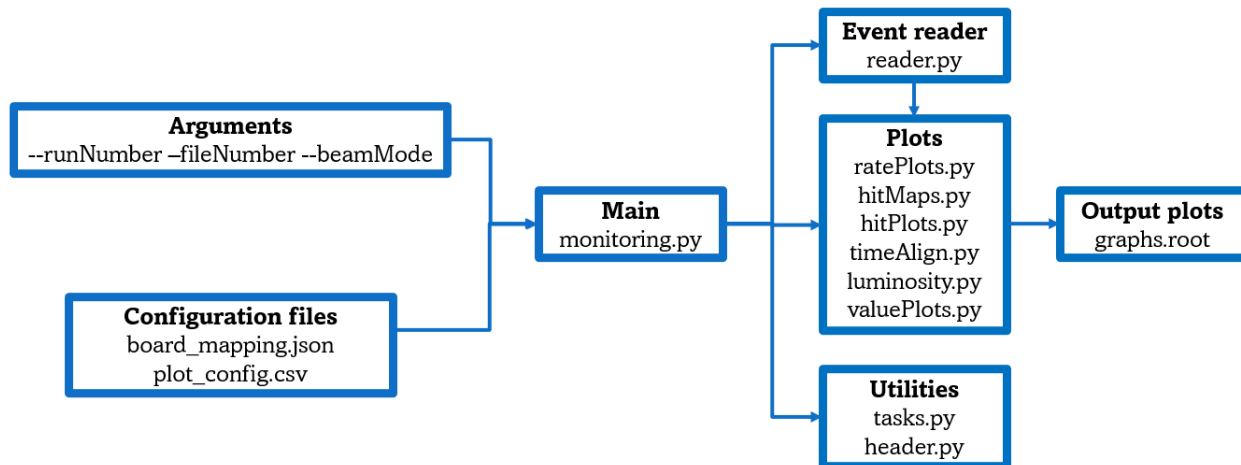


Figure 3.4: The structure of the RTDQM: the main script initializes variables, reads the desired plots from a CSV file and creates a thread for each one.

3.4 Monitoring

Several monitoring plots are available, each one is titled with an explanatory name followed by the last updated event number from the data file. The plot range and binning are automatically chosen based on the status of the LHC beams, enhancing visualization.

The “rate plot” category shows the rate of events recorded by particular combinations of subdetectors, from the single DAQ board to the whole electronic detector (Figure 3.5). Once the time range is exceeded, the graph is refreshed and the time is set back to zero.

The instantaneous luminosity at the ATLAS Interaction Point is retrieved thanks to the `pydim` module [28], then it is displayed using the same settings used for the event rates (Figure 3.6). This feature is particularly relevant, since the total event rate should follow the trend of the instantaneous luminosity. If not, it is a symptom of missing data. Once the time range is exceeded, the graph is refreshed and the time is set back to zero.

The “hit plot” category displays histograms that compare the number of hits registered in selected channels, DAQ boards or planes (Figure 3.7). This plots can be used to check for dead channels or underperforming ones (a symptom of thresholds set too high).

The “hit map” category displays 2D histograms of channels in X-axis versus Y-axis. It is used for planes with XY readout, i.e. SciFi and DS. One application of these plots is to locate the beam centroid and beam spread during a test beam (Figure 3.8).

The “alignment plots” category compares between different DAQ boards the hit timestamps inside the event window (Figure 3.9). This allows for a preliminary assessment of the correct clock synchronization of the DAQ boards. Hit timestamps refer to cycles of a 160 MHz clock, four times the LHC clock frequency. Thus, hits collected from all boards and assigned to the same event should lie within 4 timestamp cycles in order to avoid split events.

The “value plot” category displays the QDC, digitized integrated charge of SiPMs, distribution for a selected plane side (Figure 3.10). This is used to check for signal saturation (hinted by an accumulation at the end of the range). Scatter plots are available to check for correlation in QDC between sides of one plane or different ones.

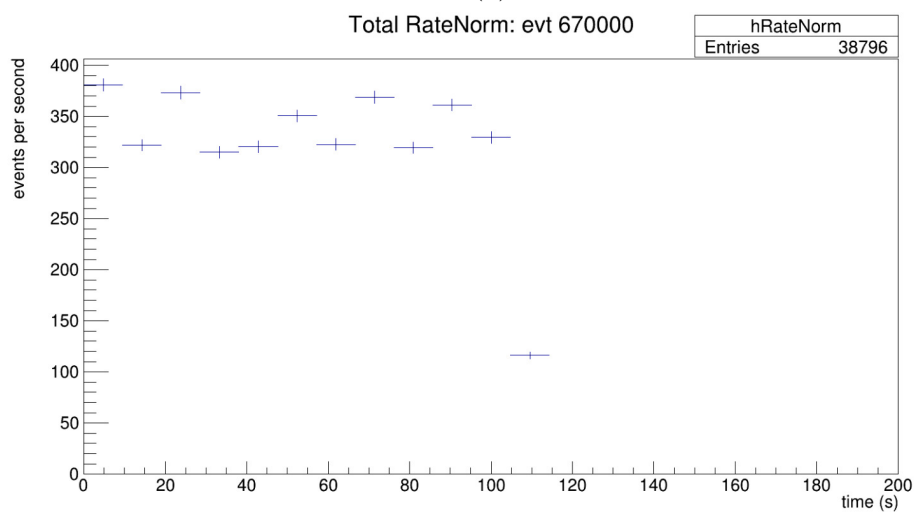
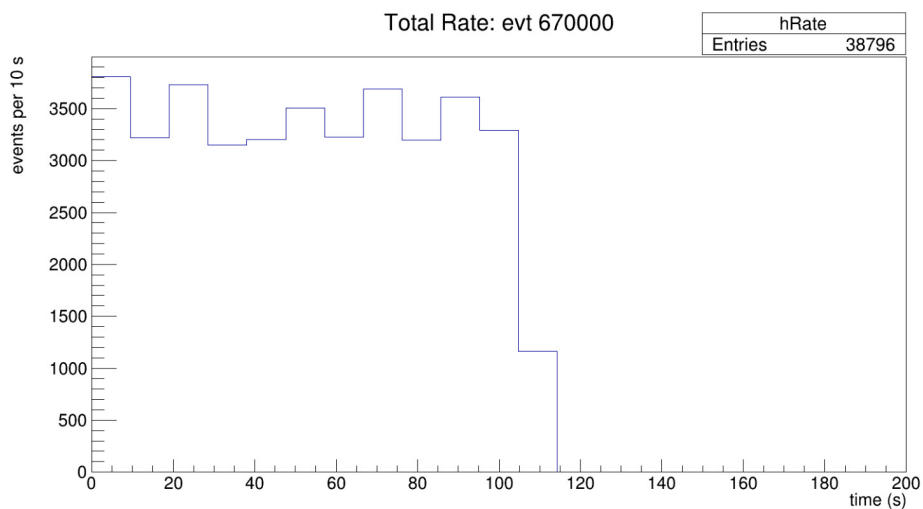


Figure 3.5: Total event rate of the electronic detector, displayed as events per bin (a) or events per second (b).

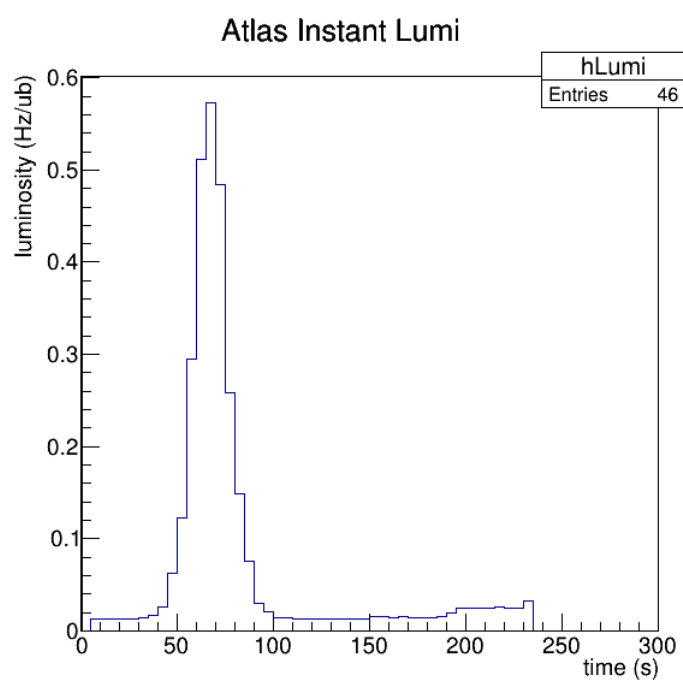
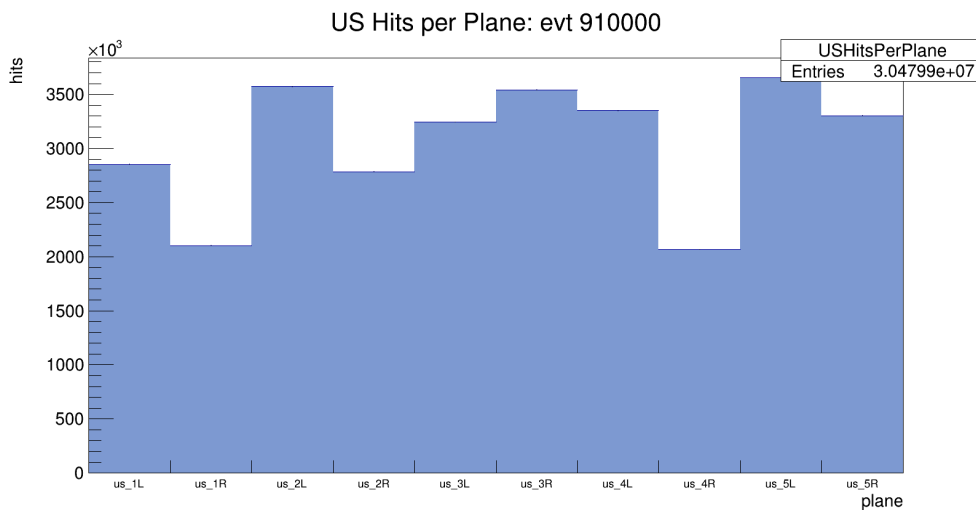
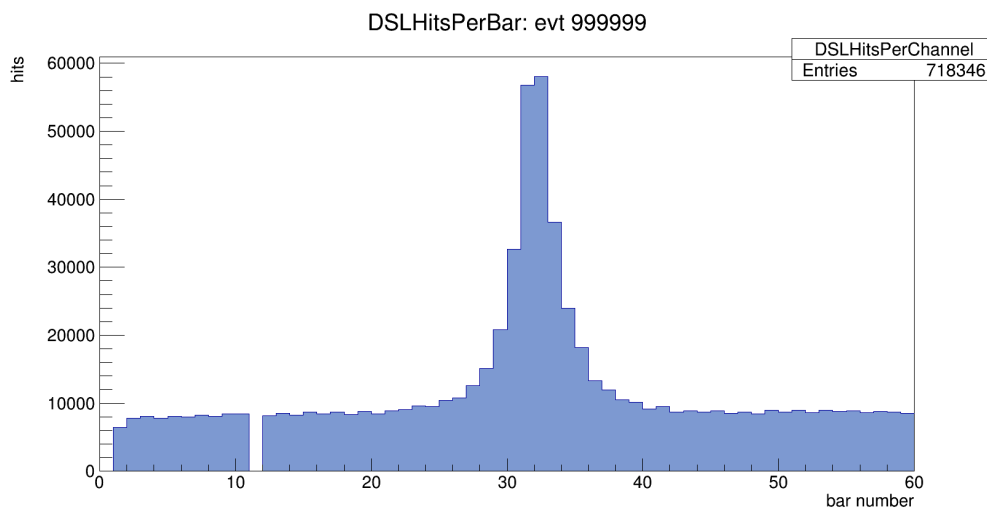


Figure 3.6: Monitor of the luminosity of ATLAS Interaction Point. Here is shown a failed attempt to provide stable beam, resulting in an early beam dump.



(a)



(b)

Figure 3.7: (a) Number of hits per UpStream plane, split into left and right side. (b) Number of hits per channel for a DownStream horizontal plane. The peak in the plot clearly shows the muon beam used during the July-August 2023 test beam. Moreover, the TOFPET channel corresponding to bar number 11 is dead or masked.

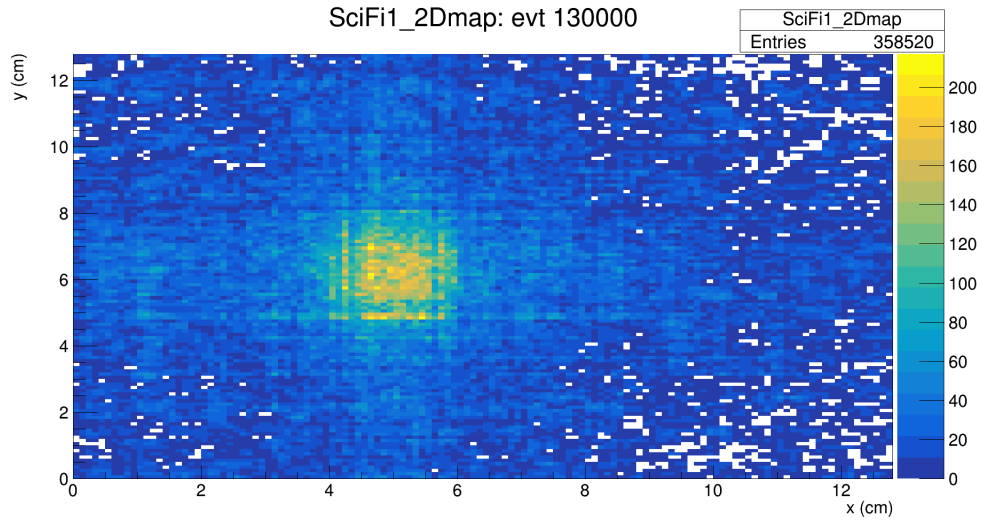


Figure 3.8: 2D map of hits in the first SciFi station, in the plot it is possible to see the beam centroid and beam spread.

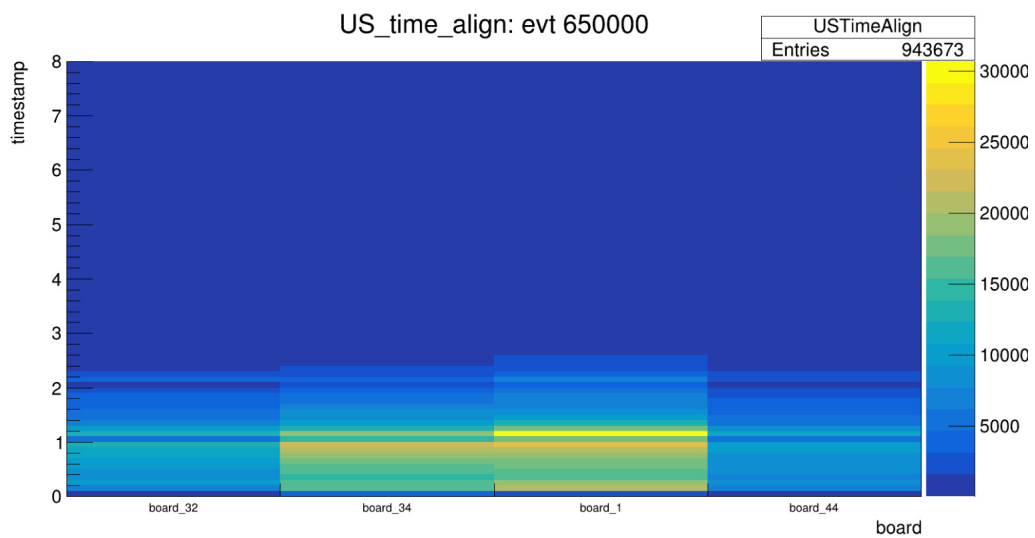


Figure 3.9: Event timestamp comparison between UpStream DAQ boards, checks for clock synchronization. The timestamp is referred to the 160 MHz LHC clock cycle, the whole event should be contained within 4 clock cycles (25 ns).

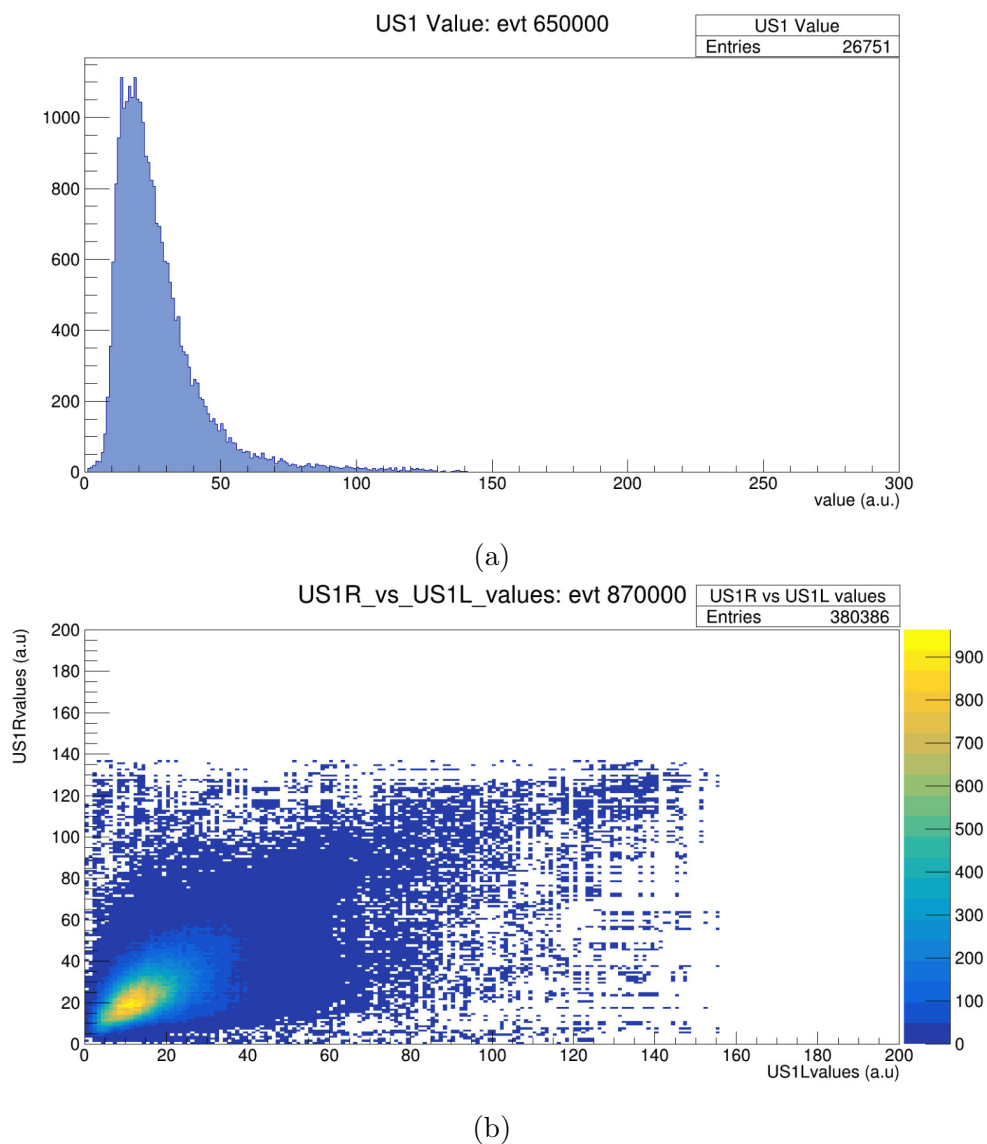


Figure 3.10: (a) QDC distribution of SiPMs in the first US station, no signal saturation is present. (b) Scatter plot for correlations in QDC between left and right side of the first US station.

Chapter 4

Test Beam Setup and Preliminary Analysis

This chapter will present the setup prepared for the SND@LHC test beam in August 2023 and my contribution to a preliminary analysis of the obtained data. The SND@LHC hadronic calorimeter is a non-compensating sampling calorimeter. The purpose of this test beam is the calibration of the SND@LHC calorimeter response as function of the hadron shower energy and of the shower origin in the target. Indeed, this is very important for the analysis of neutrino-nucleon interactions in the SND@LHC target which always produce a hadron shower. While the RTDQM was used during the test beam, the plots obtained in 4.2 and 4.3 are produced with a dedicated C++ script that I wrote for this analysis. The experimental setup, shown in Figure 4.2, consist in (following the beam direction):

- 4 Photomultipliers acting as beam monitor;
- 4 XY pairs of SciFi planes, interleaved with 10 cm removable iron slabs, the target;
- 5 US stations, interleaved with 20 cm iron slabs;
- 1 DS station.

All the electronics for the data acquisition is the same as described in Section 2.2.3 for the SND@LHC detector. Data was collected with muons and pions at selected energies between 100 GeV and 300 GeV. Three different configurations of the target were used: with 1 or 2 or 3 iron slabs.

4.1 SiPM thresholds and calibration

The TOFPET electronics for the SiPM readout, described in Section 2.2.3, needs proper calibration and threshold settings. I participated in this procedure using the tools

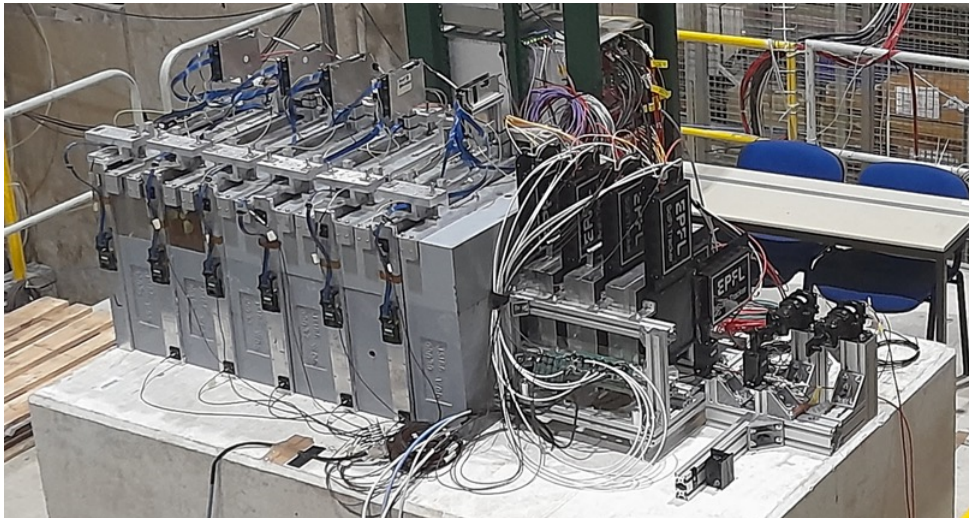


Figure 4.1: Picture of the test beam experimental setup. Going from right to left: beam counter, 4 XY pairs of SciFi planes, 5 US stations and 1 DS station.

provided by the SND@LHC calibration software. Three voltage mode discriminators with configurable thresholds are used for timing measurements, to reject low amplitude pulses, to start the charge integration window, and to trigger the event data readout. Each channel has Time to Digital Converters (TDCs) with time binning of 30 ps and charge integration Analog to Digital Converters (ADCs) with linear response up to 1500 pC input charge [29]. Each TOFPET consists of 64 independent channels, each containing independent amplifiers, discriminators, ADCs and TDCs (Figure 4.2).

The branch T of the transimpedance amplifier (TIA) converts the replica of the input current I_{IN} into a voltage V_{out_T} with an adjustable gain G_T plus an offset $V_{baseline_T}$. The amplifier saturates for $V_{out_T} > V_{sat}$. V_{out_T} connects to two identical discriminators (D_{T1} and D_{T2}) whose threshold voltages (V_{th_T1} and V_{th_T2}) can be set independently. The offset $V_{baseline_T}$ is used to trim the the baseline of V_{out_T} relatively to the input of the discriminators. The branch E of the TIA is similar but the gain G_E is lower, allowing a higher range of signals before saturation, and feeds a single discriminator D_E .

The output of the 3 discriminator generates 4 trigger signals: trigger_T, trigger_Q, trigger_E and trigger_B, with logic expressions set as in Table 4.1.

The measurement mode used in SND@LHC is called “Time and QDC mode” since:

- The TDC T measures the time of the rising edge of trigger_T;
- The QDC measures the integrated charge from the rising edge of trigger_Q until the end of the integration window;
- trigger_E is used only for energy selection and the TDC E is unused.

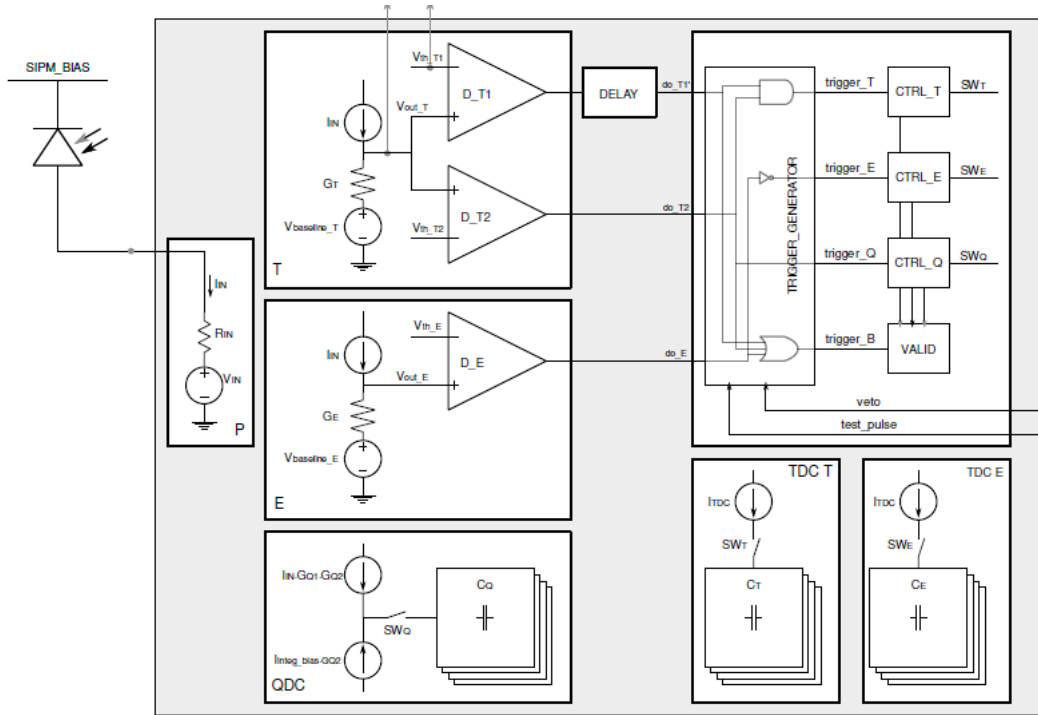


Figure 4.2: Simplified equivalent circuit of a TOFPET channel, containing amplifiers, discriminators, ADC and TDC [29].

Trigger signal	Logic expression
trigger_T	T1 and T2
trigger_Q	T2
trigger_E	not E
trigger_B	T1 or T2 or E

Table 4.1: Logic expressions for each trigger signal generated by the 3 discriminators.

4.1.1 TIA baseline and discriminators

The purpose of this procedure is to determine which setting of threshold voltage DAC (Digital to Analog Converter) corresponds to the TIA output baseline and estimate the noise in the TIA and discriminator. This procedure should be done with the sensors connected, but biased in such a way they produce no signal. Thus, SiPMs should be biased below their breakdown voltage.

The baseline adjustment (identical for T1, T2 and E) is performed by starting from an initial value of 63 DAC counts. Then, the counter is read, if the counter is less than 99.9% of maximum, then the baseline is decreased by one and the process is repeated.

Otherwise, the baseline value is found. As an example, TIA baseline calibration plots produced for the test beam are shown in Figure 4.3 for T1 and T2 and in Figure 4.4 for E.

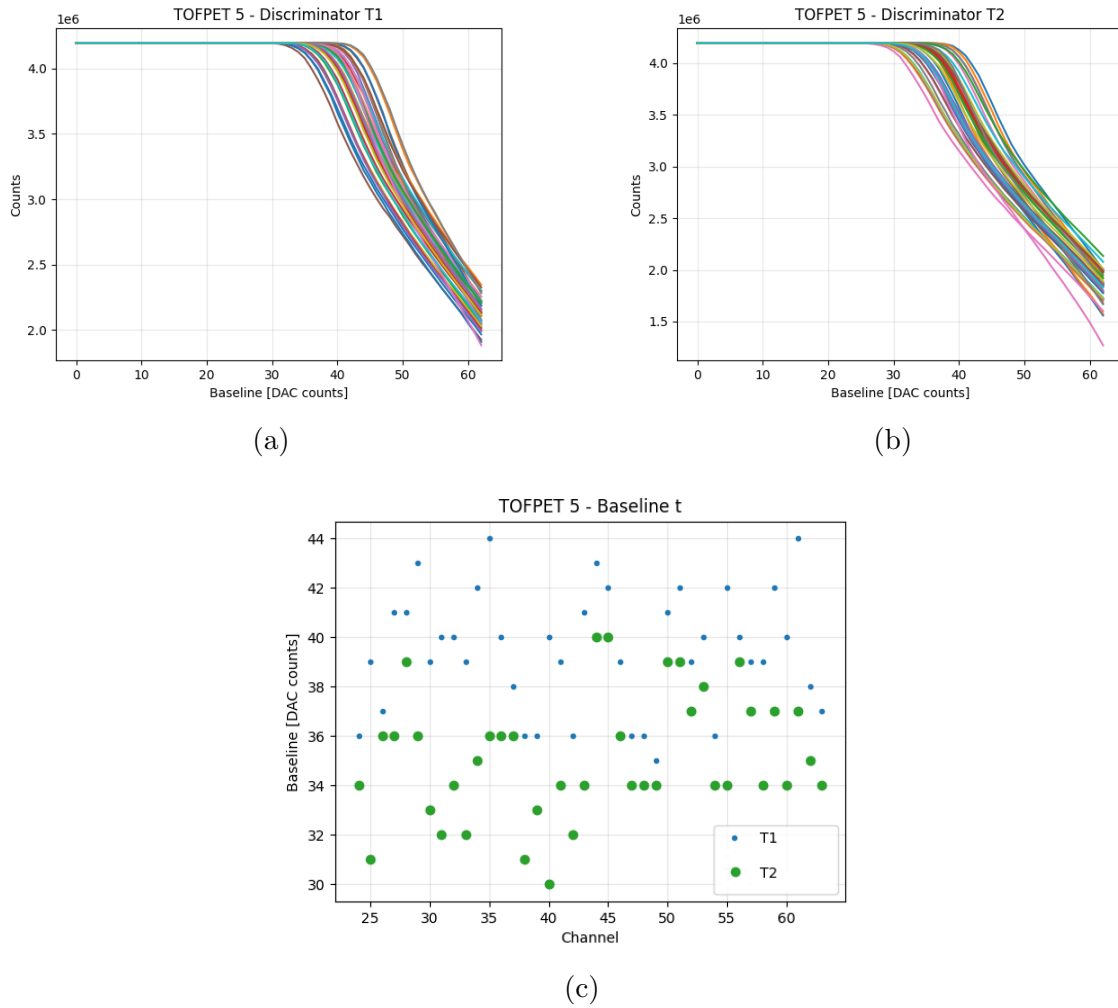


Figure 4.3: TIA baseline calibration iterations for T1 (a) and T2 (b), each line represents one TOFPET channel. The value chosen for each channel is the first one to go over 99.9% of the maximum count value, and it is reported in (c).

The threshold calibration (identical for T1, T2 and E) is performed by iterating the threshold voltages from 0 to 63 DAC counts, reading the counter at each step. The collected data is a S-curve. Fitting the cumulative distribution function to the data, the mean μ gives the position of the baseline in terms of the threshold voltage, while the standard deviation σ provides an estimate of noise. As an example, TIA thresholds

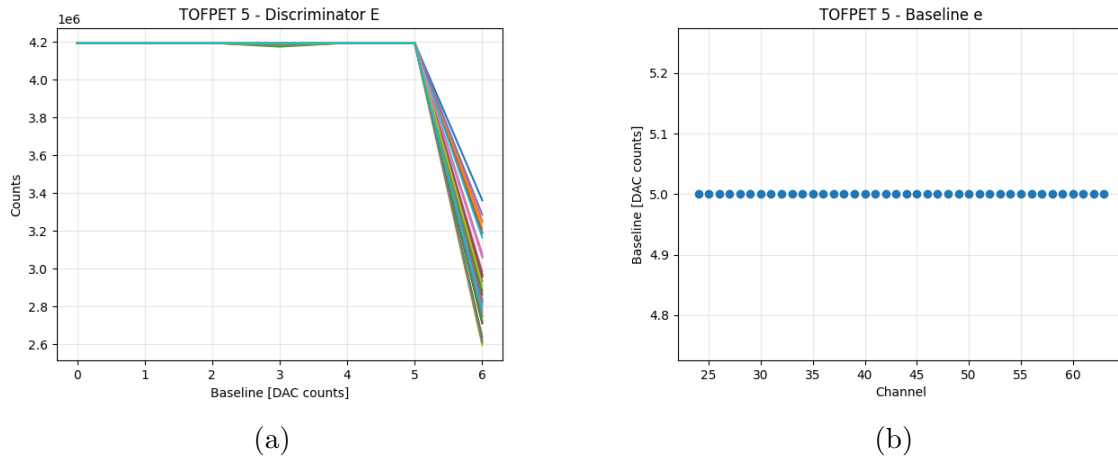


Figure 4.4: TIA baseline calibration iterations for E (a), each line represents one TOFPET channel. The value chosen for each channel is the first one to go over 99.9% of the maximum count value, and it is reported in (b).

calibrations plots produced for the test beam are shown in Figure 4.5 for T1, in Figure 4.6 for T2 and in Figure 4.7 for E.

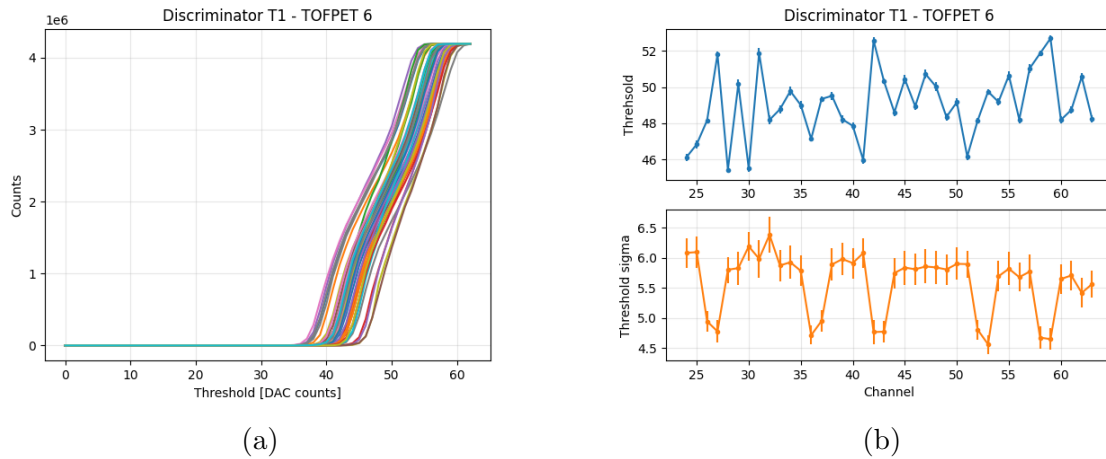


Figure 4.5: (a) Threshold baseline calibration iterations for T1, each line represents one TOFPET channel. A fit is performed on the S-curve to retrieve the mean μ and standard deviation σ of the cumulative distribution function. (b) μ and σ with their respective errors for each TOFPET channel.

Spontaneous breakdown of a Geiger-mode single-photon avalanche diode triggered by thermally generated electrons will release the same charge as when a photon is detected.

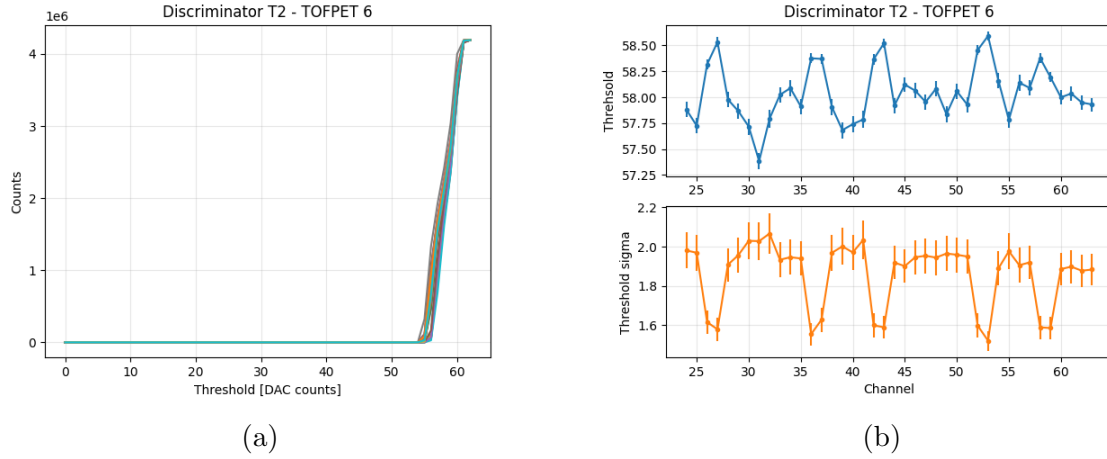


Figure 4.6: (a) Threshold baseline calibration iterations for T2, each line represents one TOFPET channel. A fit is performed on the S-curve to retrieve the mean μ and standard deviation σ of the cumulative distribution function. (b) μ and σ with their respective errors for each TOFPET channel.

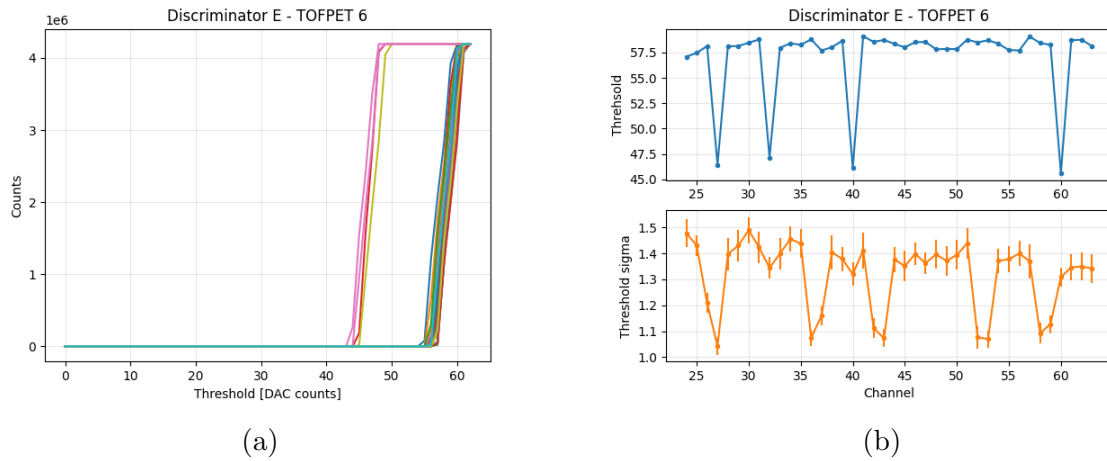


Figure 4.7: (a) Threshold baseline calibration iterations for E, each line represents one TOFPET channel. Notice that since the TOFPET belongs to a US plane, small and large SiPMs are present, as shown by the two sets of curves. A fit is performed on the S-curve to retrieve the mean μ and standard deviation σ of the cumulative distribution function. (b) μ and σ with their respective errors for each TOFPET channel.

These breakdowns are termed “dark counts” and are indistinguishable from actual photon counts. The frequency of these events is termed the “Dark Count Rate” (DCR). The internal counter can also be used to measure the DCR of the SiPM in function of threshold (Figure 4.8). The same method is used as described above but the SiPMs should be biased at the desired operation voltage.

4.1.2 TDC calibration

The purpose of this procedure is to characterize the response of the TDC as function of the trigger signal phase relative to the clock, in order to obtain a correction curve. This method uses an external signal, synchronous to the clock but with adjustable phase/delay in order to scan the phase of the trigger signal. The collected data can be fitted to a function f_{TDC} in order to extract the correction curve (Figure 4.9). The function f_{TDC} is a second-order polynomial:

$$f_{TDC}(x, a_T, b_T, c_T, d_T) = a_T[(x - d_T)\%1]^2 + b_T[(x - d_T)\%1] + c_T, \quad (4.1)$$

where the % symbol stands for the remainder of the quotient. This TDC calibration is required to obtain the precise timestamp of each hit, which is calculated using t_c , which is the coarse timestamp of the hit measured in clock cycles, and t_{fine} , which contains the raw value of the charge digitized by the TDC. Thus the timestamp t is calculated as

$$t = t_c + g_{TDC}(t_{fine}, a_T, b_T, c_T, d_T), \quad (4.2)$$

where

$$g_{TDC}(t_{fine}, a_T, b_T, c_T, d_T) = \frac{-b_T - \sqrt{b_T^2 - 4a_T(c_T - t_{fine})}}{2a_T} + d_T. \quad (4.3)$$

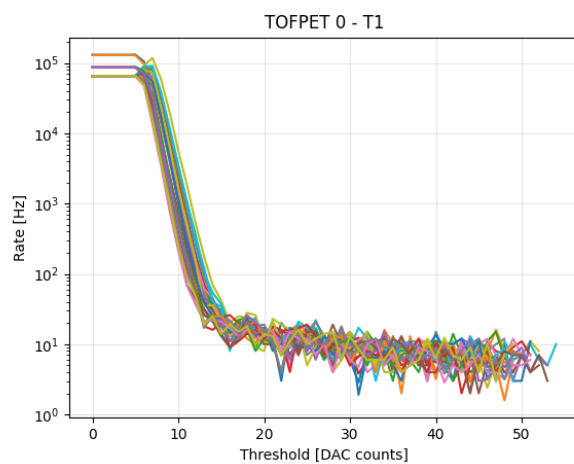
4.1.3 QDC calibration

The purpose of this procedure is to characterize the response of the QDC response as function of the integration time and integrated charge. This method uses an external signal, synchronous to the clock but with adjustable phase/delay and length to scan the integration window duration. The collected data can be fitted to a function f_{QDC} in order to extract the correction curve (Figure 4.10). The function f_{QDC} is parameterized as:

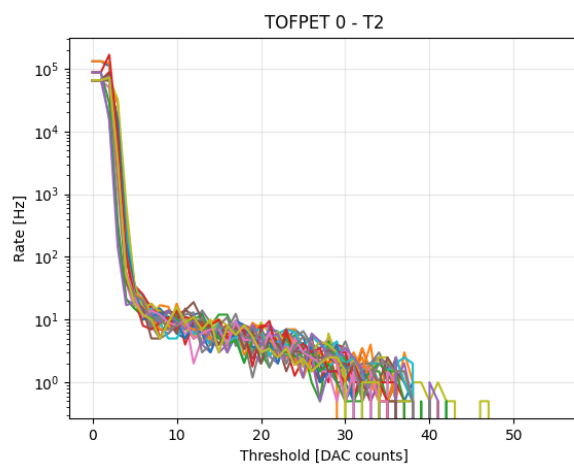
$$f_{QDC}(x, a_Q, b_Q, c_Q, d_Q, e_Q) = -c \log [1 + e^{a_Q(x-e_Q)^2 - b_Q(x-e_Q)}] + d_Q. \quad (4.4)$$

Given that v_{fine} contains the charge value digitized by the QDC and v_c is the integration time (in 160 MHz clock cycles), the calibrated QDC value is calculated as

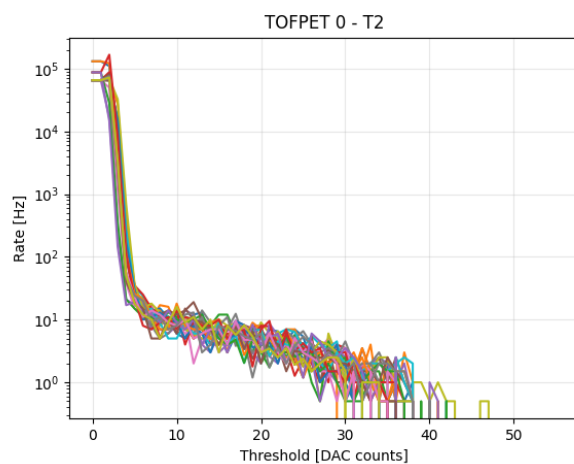
$$value = \frac{v_f - f_{QDC}(x, a_Q, b_Q, c_Q, d_Q, e_Q)}{G_{QDC}}, \quad (4.5)$$



(a)



(b)



(c)

Figure 4.8: Dark Count Rate shown in log scale as a function of the thresholds T1 (a), T2 (b) and E (c).

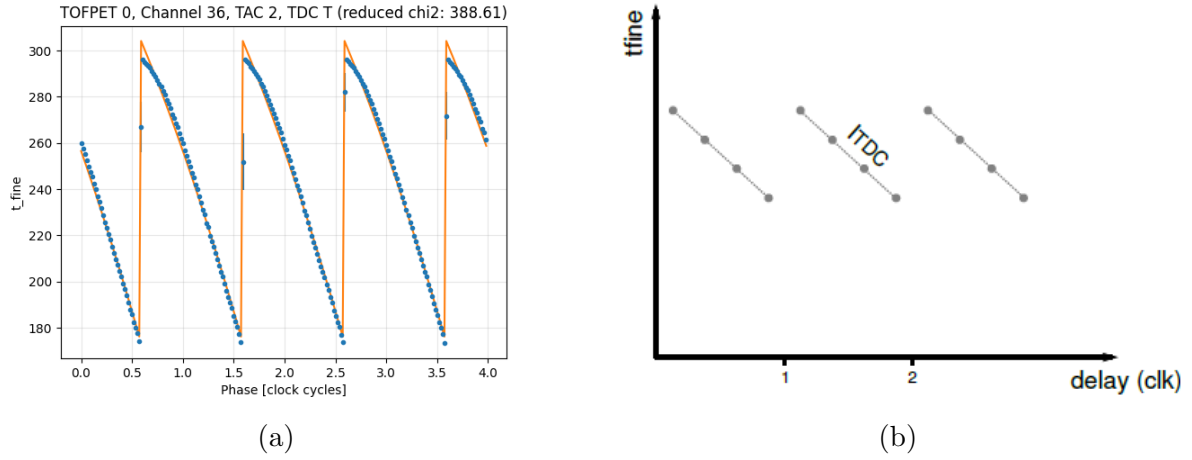


Figure 4.9: (a) t_{fine} (raw QDC value measured by the TDC) as a function of the clock phase, fitted with Equation 4.1 to retrieve the calibration parameters. (b) Expected plot provided by the TOFPET manual [29].

where $x = v_c - f_{TDC}(t_{fine}, a_T, b_T, c_T, d_T)$ and G_{QDC} is the QDC gain (ranging from 1.0 to 3.6), which in the SND@LHC detector is set to 2.5 for the best resolution and dynamic range.

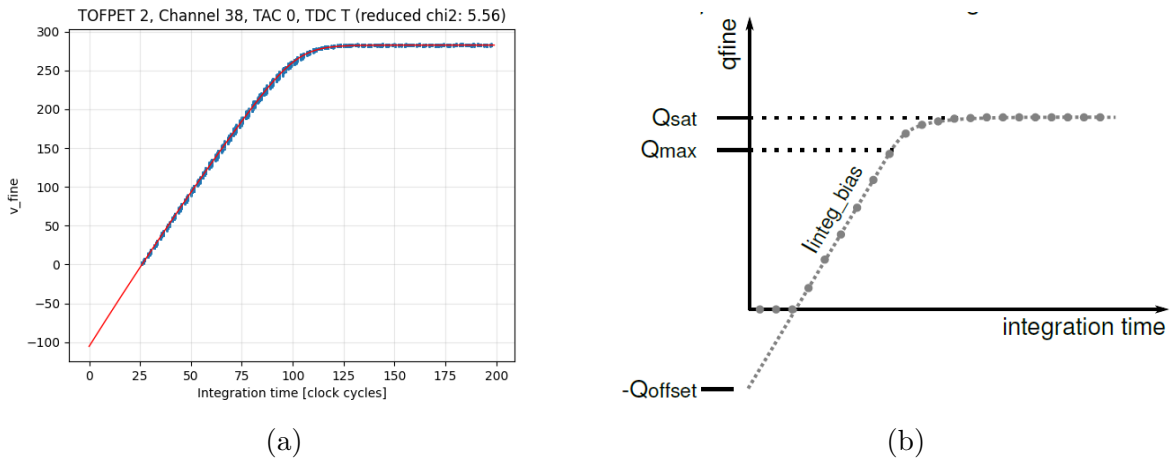


Figure 4.10: (a) v_{fine} (raw digitized charge measured by the QDC) as a function of the integration time, fitted with Equation 4.5 to retrieve the calibration parameters. (b) Expected plot provided by the TOFPET manual [29].

4.2 Muons

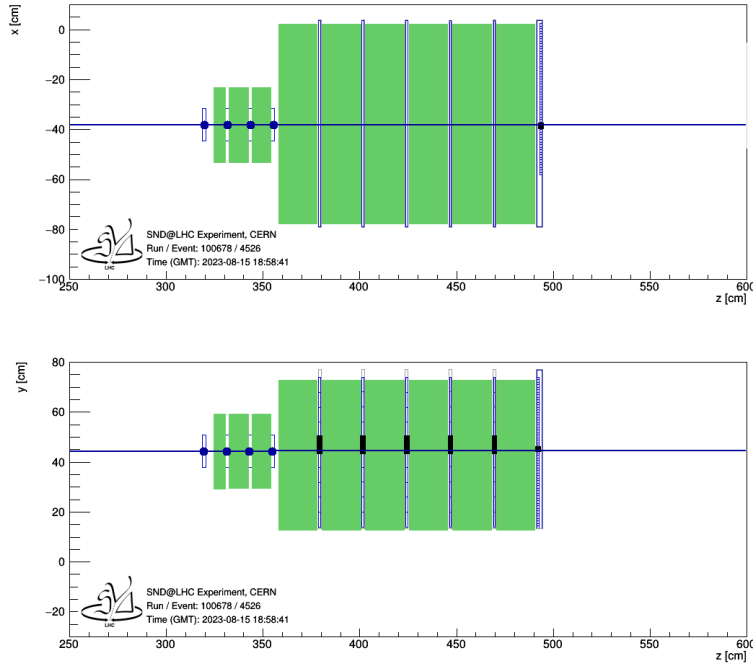


Figure 4.11: Event display of a reconstructed 160 GeV muon track. The bars which recorded a hit are marked in black, the fired SciFi channels are marked with a blue dot. The green rectangles are iron walls. The XZ plane does not present hits in the US stations since they are segmented only horizontally.

Muons are considered the best representatives for Minimum Ionizing Particles (MIPs). This means that the energy loss in a medium, described by the Bethe-Bloch formula, is close to the minimum or to the relativistic raise (which is logarithmic, thus not really different from the minimum). Muons are often used in the calibration of a detector because, being MIPs, they do not produce particle showers (except through deep inelastic scattering or through bremsstrahlung, at very high energies). Thus, muons leave a clean signal in the detector which can be used for alignment and calibration of the electronics. A 160 GeV muon beam is studied in this section, with a sample of 2.0×10^7 events. In order to reduce electronic noise, a cut is applied to the sample, requiring:

- a successfully reconstructed track, considering hits from every detector station;
- at least one hit in both SciFi1X and SciFi1Y, to select muons coming from the beam;

- narrow down the QDC signal to just one SiPMs present in the fifth US bar of each plane, where the test beam was centered, with SiPMs firing from both sides, to follow the muon track along the beam axis;
- a QDC value in the horizontal DS plane higher than 10 (above noise level), to avoid contamination with pions (which are absorbed by the iron layers in SciFi and US and cannot reach the DS station).

Applying this cut, the data sample is reduced to 9.7×10^5 events, $\sim 5\%$ of the original size. An example of an event passing this cut is show in Figure 4.11 with the event display provided by the SND@LHC analysis software [30].

The QDC distribution of one SiPMs present in the fifth US bar (corresponding to the test beam axis) is shown for each plane (split into left and right side) in Figure 4.12 and Figure 4.13. From each distribution the Most Probable Value (MPV) is retrieved, representing the MIP QDC peak. The results are summed up in Table 4.2, with an associated error corresponding to the QDC bin width. Negative QDC values are allowed due to the QDC calibration procedure described in Section 4.5.

Station	QDC MIP peak (a.u.)
US1L	1.0 ± 0.3
US1R	-1.2 ± 0.3
US2L	1.0 ± 0.3
US2R	3.0 ± 0.3
US3L	0.1 ± 0.3
US3R	4.6 ± 0.3
US4L	4.2 ± 0.3
US4R	-1.2 ± 0.3
US5L	2.3 ± 0.3
US5R	2.6 ± 0.3

Table 4.2: Most Probable Value of QDC distributions for each UpStream station, split into left and right side. The associated error corresponds to the bin width of the histograms.

In order to ensure that the fired SiPMs are measuring signal and not noise, it is interesting to look at the correlation between the QDC values measured by a left and right side SiPM in each plane. Indeed in Figure 4.14 is shown that the correlations are quite linear (with some saturation at high QDC values), due to the presence of a muon track.

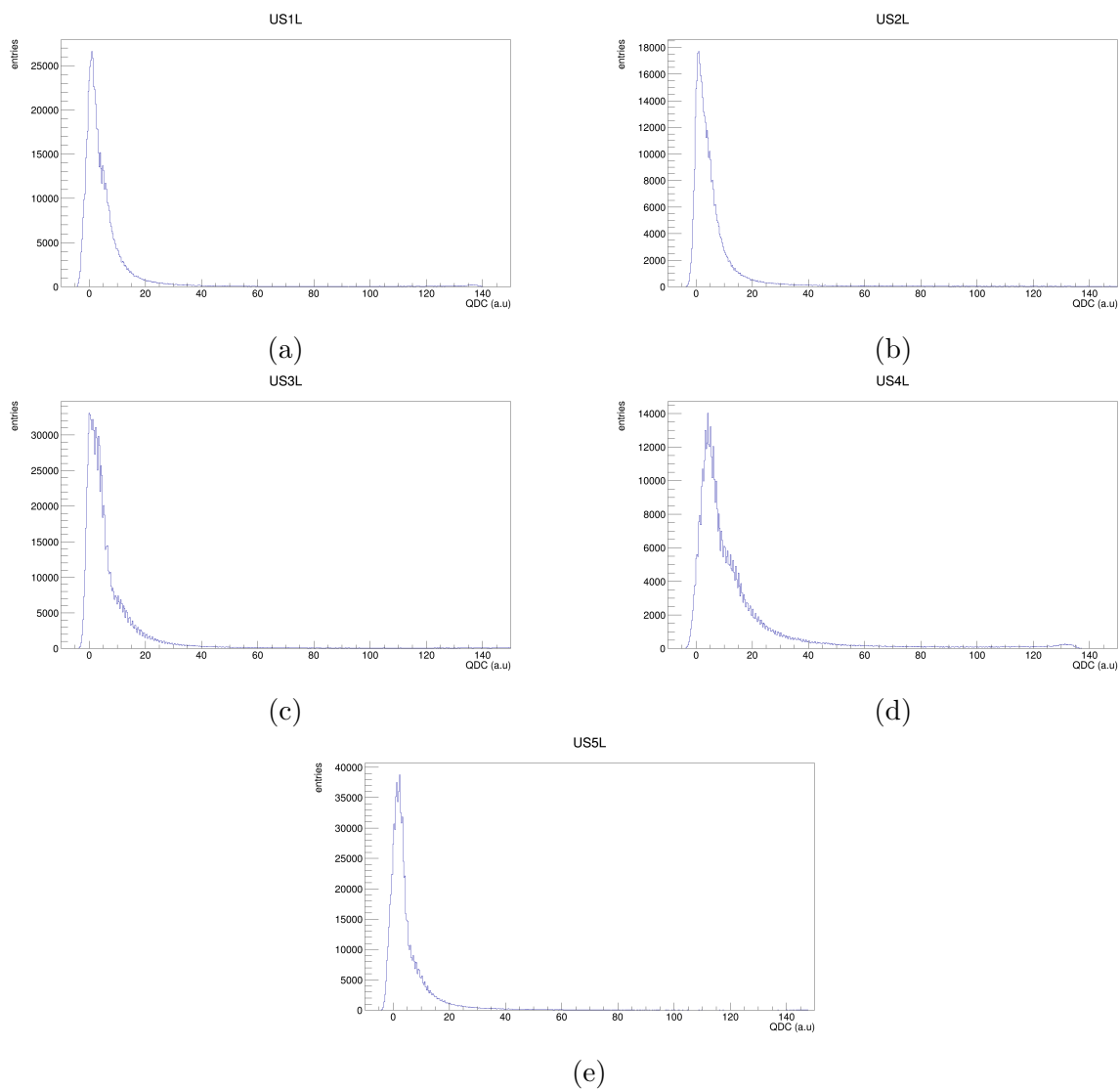


Figure 4.12: QDC distributions for each US plane (left side), small negative tails are allowed due to the QDC calibration described in Section 4.5

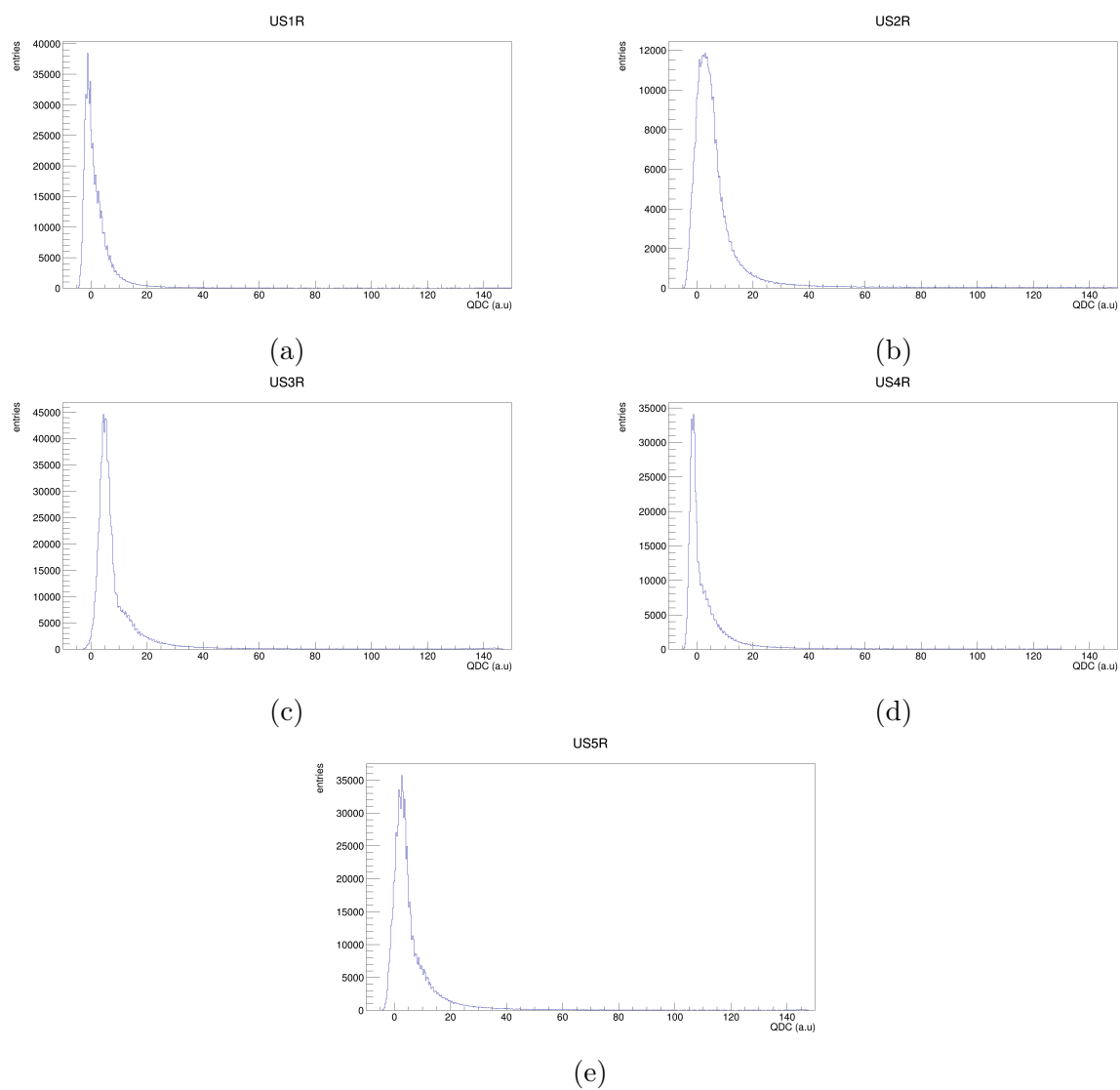


Figure 4.13: QDC distributions for each UpStream plane (right side), small negative tails are allowed due to the QDC calibration described in Section 4.5

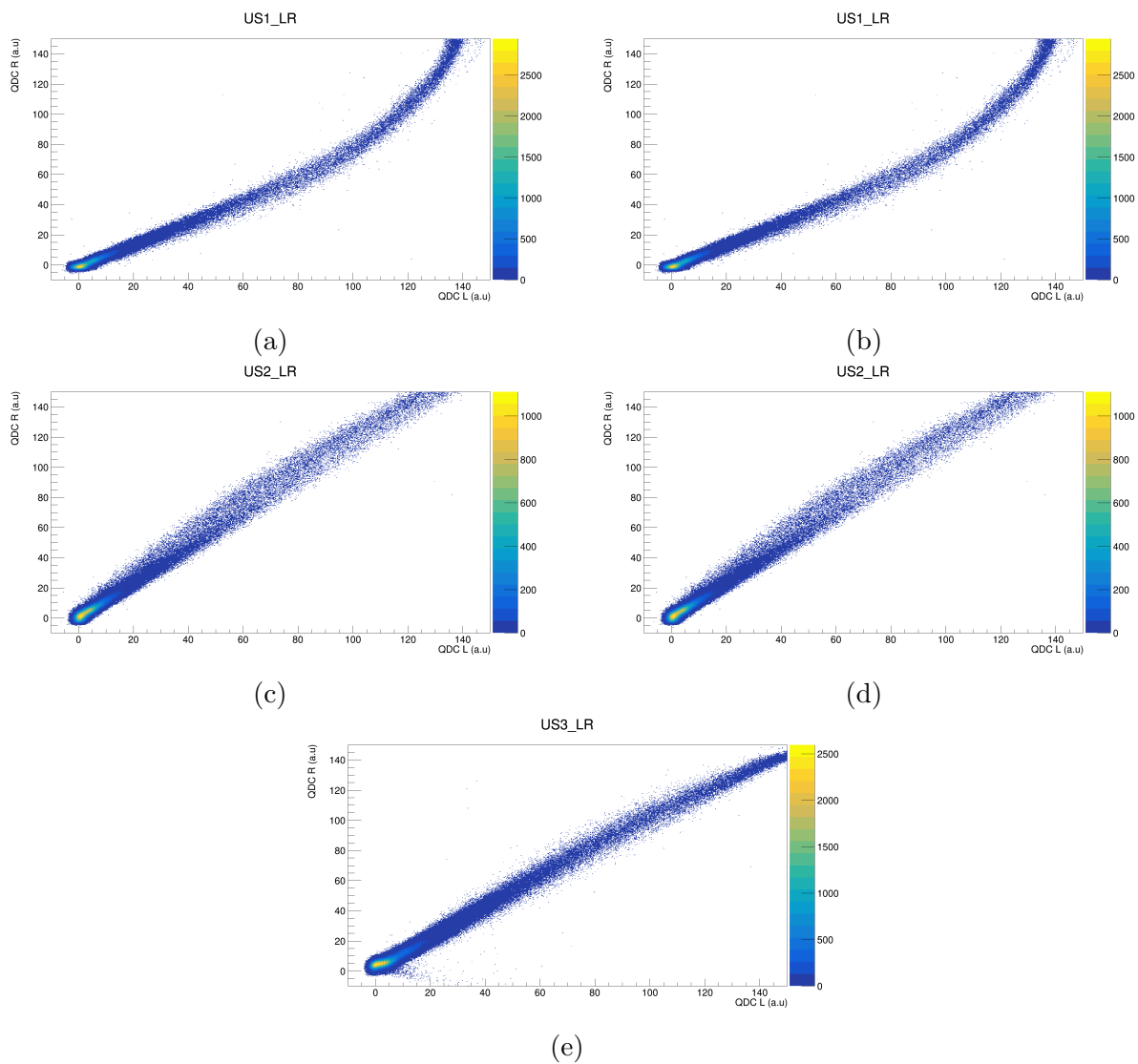


Figure 4.14: Correlations between left and right QDC measured by one SiPM for each UpStream plane. A linear correlation suggests the presence of a muon track. (a) and (b) show some saturation at high QDC values.

4.3 Pions

A highly-energetic pion interacting with a nucleus produces a large number of secondary hadrons. They deposit energy through ionization/excitation of the medium and through successive interactions with nuclei yielding lower energy hadrons, the hadronic shower. Neutral mesons produced in the shower, mainly π^0 , immediately decay into a $\gamma\gamma$ pair. In matter, each high-energy photon converts into an electron-positron pair, each able to radiate energetic photons through bremsstrahlung. These radiated photons can convert into pairs that, in turn, radiate. In conclusion, in an hadronic shower there is also an electromagnetic shower with a large number of photons, electrons, and positrons.

During the test beam, several pion energies and target configurations were explored. Three different configurations of the target were used: with 1 or 2 or 3 iron slabs. All the configurations with the correspondent amount of events used for this analysis are shown in Table 4.3. In order to isolate events with particles coming from the beam, events which do not present at least 7 (out of 8) SciFi planes fired, are discarded. The fraction of events passing the cut are shown in the last column of Table 4.3. An example of an 100 GeV pion event passing this cut is show in Figure 4.15 with the event display provided by the SND@LHC analysis software [30].

Particle	Energy (GeV)	Iron blocks	events	Fraction passing cut
π^+	100	3	2.0×10^7	0.274
π^+	100	2	1.5×10^7	0.267
π^+	100	1	1.5×10^7	0.325
π^+	140	3	2.0×10^7	0.541
π^+	140	2	1.5×10^7	0.528
π^+	140	1	1.5×10^7	0.401
π^+	180	3	2.0×10^7	0.128
π^+	180	2	1.5×10^7	0.121
π^+	180	1	1.5×10^7	0.164
π^-	240	3	2.0×10^7	0.109
π^-	240	2	1.5×10^7	0.123
π^-	240	1	1.5×10^7	0.144
π^-	300	3	2.0×10^7	0.096
π^-	300	2	1.5×10^7	0.103
π^-	300	1	1.5×10^7	0.139

Table 4.3: Data sample used in this analysis. Several pion energies and target configurations were explored. Three different configurations of the target were used: with 1 or 2 or 3 iron slabs. The last column shows the fraction of events passing the selection cut.

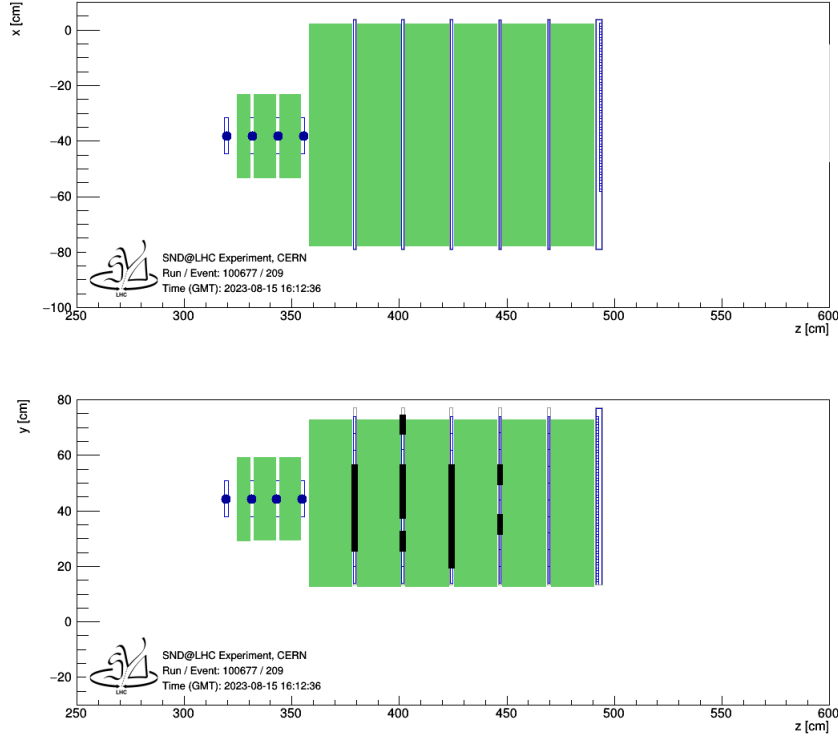


Figure 4.15: Event display of a 100 GeV pion event with 3 iron block present in the target. The bars which recorded a hit are marked in black, the fired SciFi channels are marked with a blue dot. The green rectangles are iron walls. The XZ plane does not present hits in the US stations since they are segmented only horizontally. In this event the pion passes through the whole SciFi system and begins the shower in the first wall of the muon system.

An immediate check on the relevance of the target configuration can be performed by looking at the beam profile, on both axis, thanks to SciFi planes. The first SciFi plane shows the beam position and width while the SciFi plane just after the first iron block (the position depends on the target configuration) presents some broadening and increase in the number of hits due to showering (Figure 4.16).

SciFi can trace back the iron block in which the pion began the shower by monitoring the number of hits n_{hits} in each SciFi plane. Indeed, it is observed a clear change (from $n_{hits} < 10$ hits to $n_{hits} > 100$) between two consecutive planes. By imposing $n_{hits} > 20$ as a condition for the starting point of a shower, a probability distribution of the starting iron block (if any) of a shower is obtained (Figure 4.16). It is shown that even with the full target present, $\gtrsim 20\%$ of pions pass through the iron blocks in SciFi without showering. An anomalous behaviour is present for the 140 GeV pions, which seem to

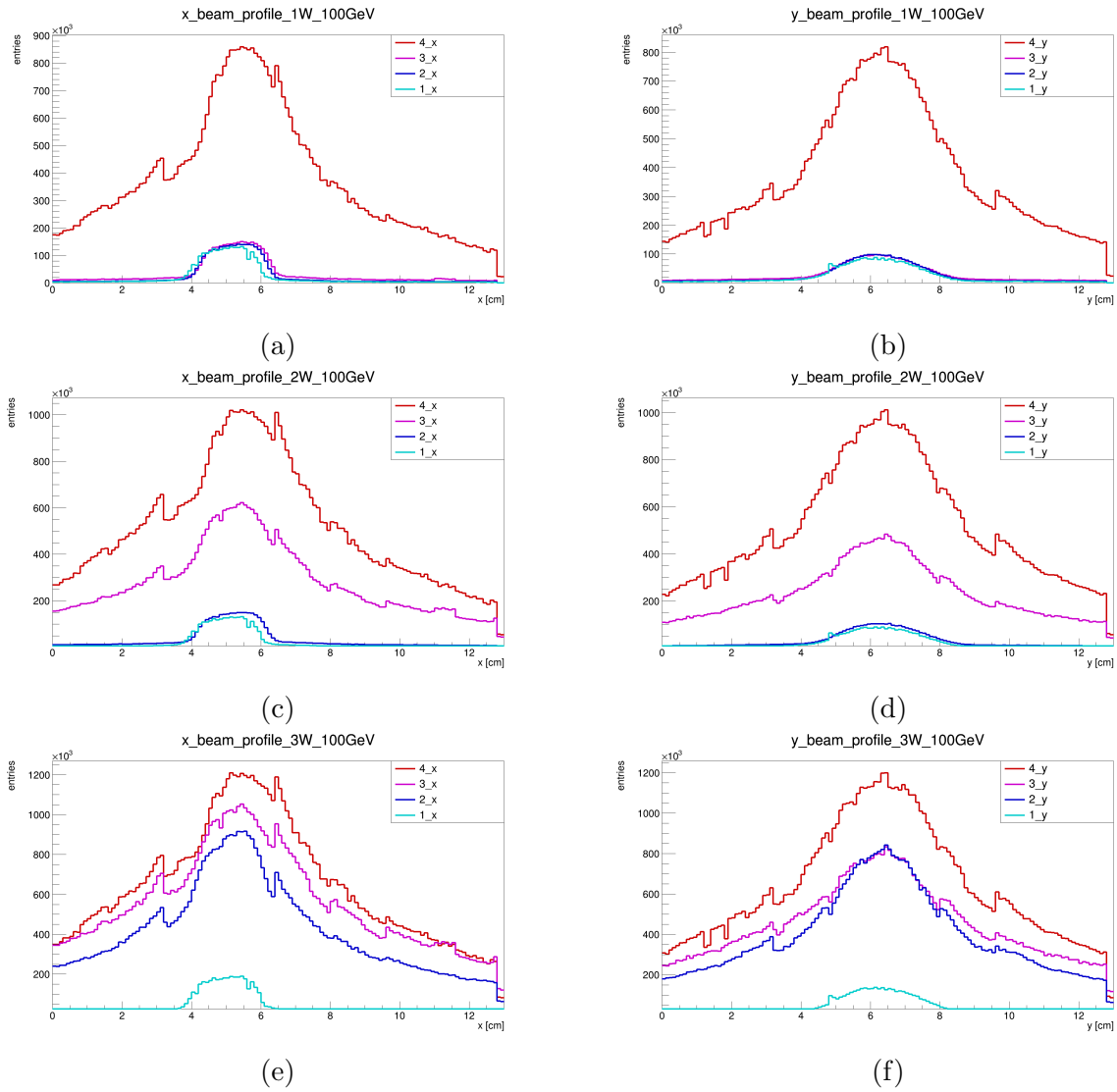
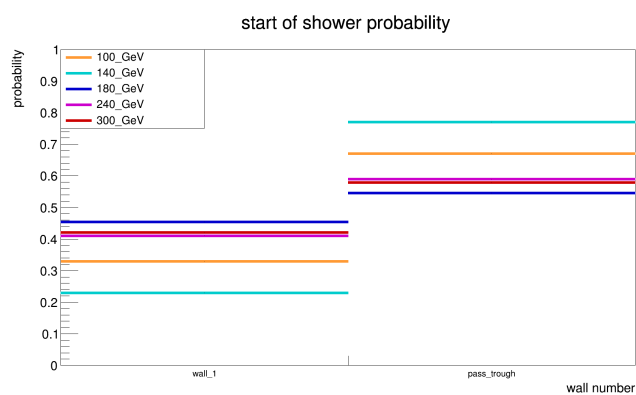


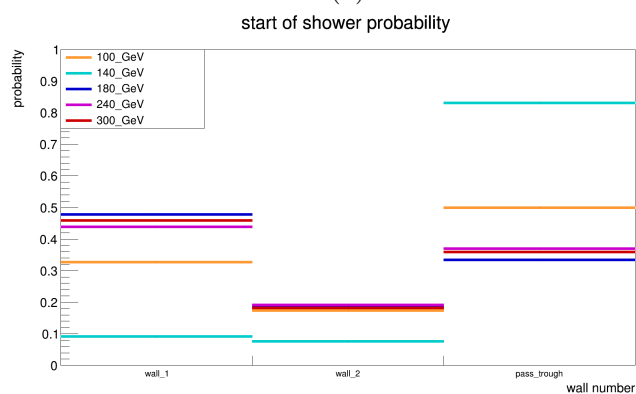
Figure 4.16: Shower profile (X on the left and Y on the right) in the target generated by 100 GeV pions. In (a) and (b) only one iron wall is present in the target, two in (c) and (d), three in (e) and (f). Each histogram represents data collected by each SciFi plane, from 1 to 4.

interact in the target with less probability, which is being investigated.

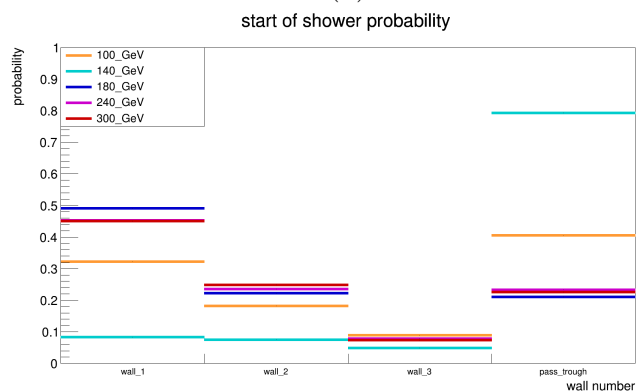
Now, while the relevant observable for SciFi is n_{hits} , for the US system the analysis revolves around the QDC. Looking at the distributions of QDC collected by one plane in an event, the showers generated by pions with higher energy reach higher QDC values, as expected. In Figure 4.18 these distributions are shown for each plane with a target configuration consisting in one iron block. At the time of writing this thesis, the analysis is still going on. However, what has been shown gives clear indications of the good sensitivity that the number of hits in the SciFi system and the QDC values in the US system have to the shower energy and to the location of its origin along the target.



(a)



(b)



(c)

Figure 4.17: Probability distribution for which iron wall contains the starting point of the pion shower. Five different pion energies are compared, for each target configuration. Even with the full target (3 iron slabs) present, $\sim 20\%$ of pions pass through the iron blocks without showering.

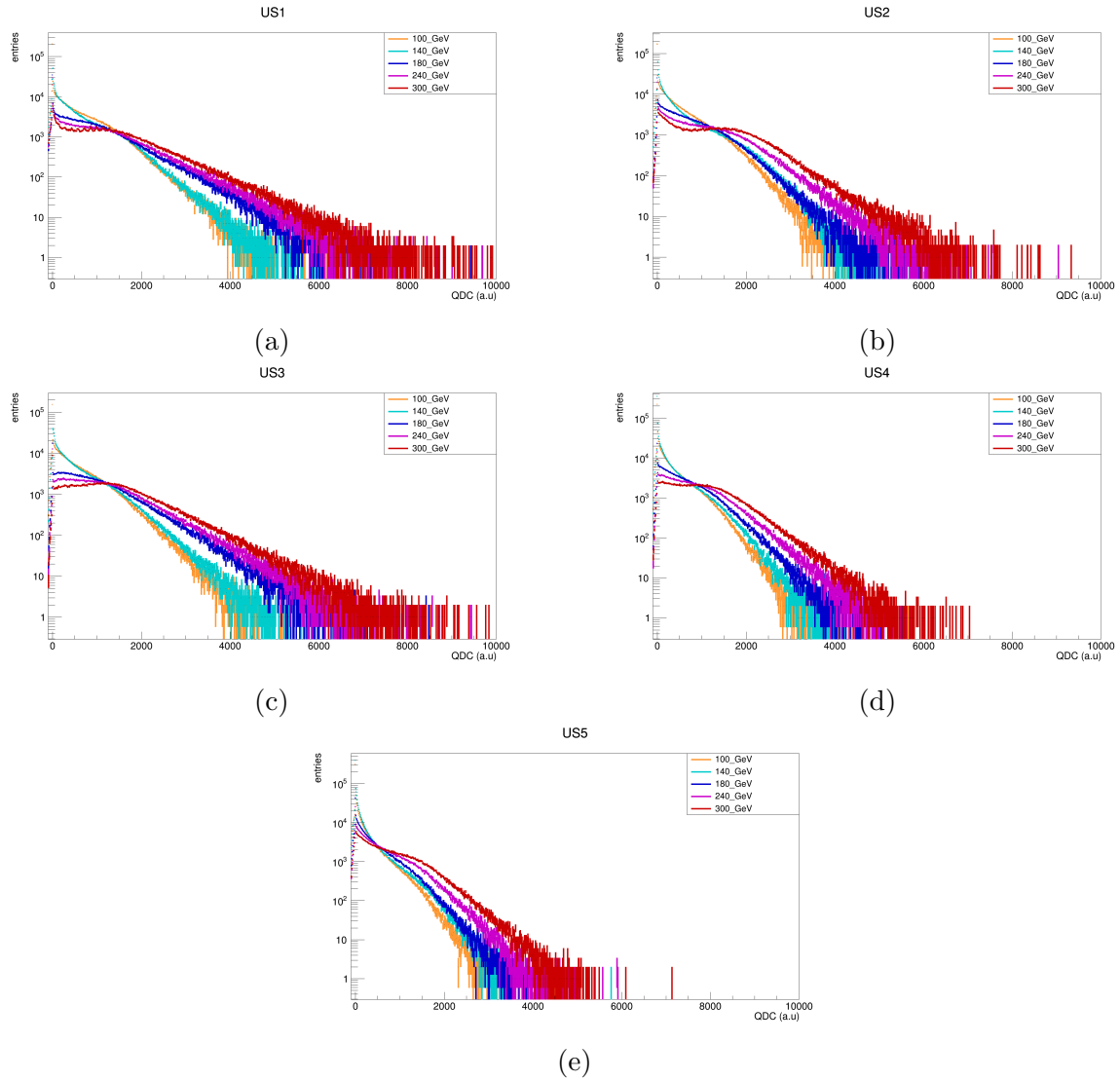


Figure 4.18: QDC distribution for every US plane, compared for pions with different energies. The number of entries is rescaled to balance out the different number of selected events for different energies. The plot show that the QDC distribution of hadron showers generated by pions with higher energies leans towards higher QDC values.

Conclusions

SND@LHC is a hybrid detector located 480 m downstream of the ATLAS Interaction Point (IP) that allows for the identification of all three neutrino flavours through nuclear emulsion films and scintillating fibers/bars. It will study for the first time neutrinos of energies up to a few TeV, making the bridge to astrophysical measurements. In this thesis work I developed a multi-threaded Python software for the real time monitoring of the SND@LHC electronic detector. This Real Time Data Quality Monitor (RTDQM) has been integrated as a subsystem of the SND@LHC Experiment Control System. The RTDQM performs quality checks, detector performance checks, and a first online analysis on the collected data. Moreover, it is able to retrieve the luminosity measured in the ATLAS IP and the beam status, in order to adapt automatically to the best plotting parameters for the best graph visualization. The RTDQM can be operated through a simple Graphical User Interface, which allows to select the desired monitoring plots. The source code is public and available on GitHub (https://github.com/FelixofRivia/SNDatLHC_RTQDM). This tool was extensively used during a test beam in July-August 2023 devoted to the calibration of the SND@LHC calorimeter for measuring the energy of hadronic showers. This is essential for the analysis of neutrino-nucleon interactions, which always produce a hadronic shower. I presented a preliminary analysis of the test beam data, covering muons and pions with several energies between 100 GeV and 300 GeV, that explored the performance of the main observables for a measurement of the hadronic shower energy in SND@LHC, i.e. the number of hits in the SciFi tracker system and the QDC values in the UpStream stations of the calorimeter.

Appendix A

RTDQM main script

The main script (`monitor.py` [31]) creates threads thanks to the `threading` module. At the start of the program, the arguments passed from the command line are used to initialize global variables. The input file is prepared for event reading and all the available monitoring plots are defined through threading functions. The list of the desired functions is read from a CSV file and the corresponding threads start. The program is kept running until a system stop signal is received. Here is reported the source code of `monitor.py`.

```
1 import numpy as np
2 import argparse
3 import threading
4 import ROOT
5 import os
6 import time as t
7
8 import Scripts.header as h
9 import Scripts.tasks as task
10 import Scripts.ratePlots as r
11 import Scripts.hitPlots as hit
12 import Scripts.hitMaps as map
13 import Scripts.luminosity as lum
14 import Scripts.reader as read
15 import Scripts.valuePlots as val
16 import Scripts.timeAlign as align
17
18
19 if __name__ == '__main__':
20     parser = argparse.ArgumentParser()
21     parser.add_argument('runNumber', type=str)
22     parser.add_argument('fileNumber', type=str)
23     parser.add_argument('beammode', type=str)
24     args = parser.parse_args()
25
26     h.fileN = int(args.fileNumber)
27     h.runN = int(args.runNumber)
28
29     #make run (file) number 6 (4) digits , 0 padded
```

```

30     runNumber = args.runNumber.rjust(6,"0")
31     fileNumber = args.fileNumber.rjust(4,"0")
32     beammode = args.beammode.lower()
33     print(f"Beammode = {beammode} -----",flush=True)
34
35     TH1.AddDirectory(False)
36     # h.filedir = f"root://snd-server-1:1094//mnt/raid1/data_online/" #online
37     # h.filedir = f"/home/sndmon/QtDqmp/Data/" #local new
38     # h.filedir = f"/home/sndmon/Snd/Data/" #local old
39     h.filedir = f"/home/sndecs/RunData/" #local TB
40     # h.filedir = f"././Data/"
41     if beammode=="test":
42         h.filedir = f"./Data/" #local test
43         h.confName = "board_mapping_local.json"
44
45     h.filename = h.filedir + f"run_{runNumber}/data_{fileNumber}.root"
46
47     h.wrtfile = ROOT.TFile.Open(h.wrtfilename, "RECREATE")
48     print(f"creating write file: {h.wrtfilename}",flush=True)
49     h.wrtfile.Close()
50
51     h.file = ROOT.TFile.Open(h.filename,'r')
52
53     task.setBeamParam(beammode)
54
55     #run through all the events (recommended option)
56     task.updateAllEvents()
57
58     #start from the event arg1 seconds ago, until h.timeRange
59     #task.updateSecondsAgo(150)
60
61     #plot events between arg1 and arg2 seconds ago
62     #task.updateTimeRange(300,120)
63
64     #enable root multithreading
65     nThreads = 10
66     ROOT.EnableThreadSafety()
67     ROOT.EnableImplicitMT(nThreads)
68
69     print("To kill program, enter Ctrl+\\",flush=True)
70
71     #gROOT.SetBatch(True)
72
73     #pull board info from json file
74     task.getBoardArrays(beammode)
75
76     #define threading functions
77     reader = threading.Thread(target=read.readEntry)
78     rate = threading.Thread(target=r.plotGlobalEvtRate)
79     lumi = threading.Thread(target=lum.main)
80
81     rateVeto = threading.Thread(target=r.plotDetHitRate, args = ("Veto",h.vetoId))
82     rateSciFi = threading.Thread(target=r.plotDetHitRate, args=("SciFi",h.sciFiId))
83     rateUS = threading.Thread(target=r.plotDetHitRate, args=("US",h.usId))
84     rateDS = threading.Thread(target=r.plotDetHitRate, args=("DS",h.dsId))
85     rateBM = threading.Thread(target=r.plotDetHitRate, args=("BM",h.beammonId))
86
87     sciFiCh = threading.Thread(target=hit.plotHitsChDet, args=("SciFi",h.sciFiId,h.sciFiName))
88     vetoCh = threading.Thread(target=hit.plotHitsChannel, args=("Veto",h.vetoId))
89     usCh = threading.Thread(target=hit.plotHitsChDet, args=("US",h.usId,h.usName))
90     dsCh = threading.Thread(target=hit.plotHitsChDet, args=("DS",h.dsId,h.dsName))

```

```

91     bmCh = threading.Thread(target=hit.plotHitsChDet, args=("BM",h.beammonId,h.beammonName))
92
93     hitsTot = threading.Thread(target=hit.plotHitsBoard, args=("Total",h.totId,h.totName))
94     hitsVeto = threading.Thread(target=hit.plotHitsBoard, args=("Veto",h.vetoId,h.vetoName))
95     hitsSciFi = threading.Thread(target=hit.plotHitsBoard, args=("SciFi",h.sciFiId,h.sciFiName))
96     hitsUS = threading.Thread(target=hit.plotHitsBoard, args=("US",h.usId,h.usName))
97     hitsDS = threading.Thread(target=hit.plotHitsBoard, args=("DS",h.dsId,h.dsName))
98     hitsBM = threading.Thread(target=hit.plotHitsBoard, args=("BM",h.beammonId,h.beammonName))
99
100    hitsBarDSL = threading.Thread(target=hit.plotHitsBar, args=("DSL",h.dsId[0],[0,1]))
101    hitsBarDSR = threading.Thread(target=hit.plotHitsBar, args=("DSR",h.dsId[0],[6,7]))
102
103    mapSciFi1 = threading.Thread(target=map.plot2DSciFi,args=(h.sciFiId[0][0],h.sciFiId[1][0],"SciFi1"))
104    hitMap = threading.Thread(target=map.plot2DMap, args=(11,29,[0,1,2,3,5,6,7],[0,1,2,3,5,6,7],"SciFi_1_hitmap",1,1))
105    hitMapDSV = threading.Thread(target=map.plot2DMap, args=(48,48,[2,3],[2,3],"DSVhitmap",1,1))
106    valDS1 = threading.Thread(target=val.plotValueBoardMS, args=("DS1",h.dsId[0],[0,1,2,3,6,7]))
107    valDS1V = threading.Thread(target=val.plotValueBoardMS, args=("DS1V",h.dsId[0],[2,3]))
108    valDS1V2 = threading.Thread(target=val.plotValueBoardMS, args=("DS1V2",h.dsId[0],[2]))
109    valDS1V3 = threading.Thread(target=val.plotValueBoardMS, args=("DS1V3",h.dsId[0],[3]))
110    valDS1L = threading.Thread(target=val.plotValueBoardMS, args=("DS1L",h.dsId[0],[6,7]))
111    valDS1R = threading.Thread(target=val.plotValueBoardMS, args=("DS1R",h.dsId[0],[0,1]))
112
113
114    valUS1 = threading.Thread(target=val.plotValueBoardMS, args=("US1",h.usId[0],[4,5,6,7]))
115    valUS2 = threading.Thread(target=val.plotValueBoardMS, args=("US2",h.usId[0],[0,1,2,3]))
116    valUS3 = threading.Thread(target=val.plotValueBoardMS, args=("US3",h.usId[1],[0,1,4,5]))
117    valUS4 = threading.Thread(target=val.plotValueBoardMS, args=("US4",h.usId[2],[0,1,2,3]))
118    valUS5 = threading.Thread(target=val.plotValueBoardMS, args=("US5",h.usId[3],[0,1,2,3]))
119
120    scatValUS1 = threading.Thread(target=val.plotScatterValue, args=(h.usId[0],h.usId[0],[6,7],[4,5],"US1L","US1R"))
121    scatValUS2 = threading.Thread(target=val.plotScatterValue, args=(h.usId[0],h.usId[0],[2,3],[0,1],"US2L","US2R"))
122    scatValUS3 = threading.Thread(target=val.plotScatterValue, args=(h.usId[1],h.usId[1],[4,5],[0,1],"US3L","US3R"))
123    scatValUS4 = threading.Thread(target=val.plotScatterValue, args=(h.usId[2],h.usId[2],[2,3],[0,1],"US4L","US4R"))
124    scatValUS5 = threading.Thread(target=val.plotScatterValue, args=(h.usId[3],h.usId[3],[2,3],[0,1],"US5L","US5R"))
125    scatValUS1R2R = threading.Thread(target=val.plotScatterValue, args=(h.usId[0],h.usId[0],[4,5],[0,1],"US1R","US2R"))
126    scatValUS1L2L = threading.Thread(target=val.plotScatterValue, args=(h.usId[0],h.usId[0],[6,7],[2,3],"US1L","US2L"))
127    scatValUS1R1V = threading.Thread(target=val.plotScatterValue, args=(h.usId[0],h.dsId[0],[4,5],[2,3],"US1R","DS1V"))
128
129    alignUS = threading.Thread(target=align.plotTimeAlign, args=("US",h.usId))
130
131    planeUS = threading.Thread(target=hit.plotHitsPlaneMS, args=("US",h.usId,h.usPName, h.usSlot))
132    planeDS = threading.Thread(target=hit.plotHitsPlaneMS, args=("DS",h.dsId,h.dsPName, h.dsSlot))
133    planeSciFi= threading.Thread(target=hit.plotHitsPlaneMB, args=("SciFi",h.sciFiId,h.sciFiName))
134
135    flags = task.read_csv_file("./plot_config.csv")
136    #reader should ALWAYS be running!
137    reader.start()
138    #start threads
139
140    # rateVeto.start()
141    if task.return_flag(flags, "rateSciFi")==1:
142        rateSciFi.start()
143    if task.return_flag(flags, "rateUS")==1:
144        rateUS.start()
145    if task.return_flag(flags, "rateDS")==1:
146        rateDS.start()
147    if task.return_flag(flags, "rateBM")==1:
148        rateBM.start()
149
150    # hitsVeto.start()
151    if task.return_flag(flags, "hitsTot")==1:

```

```

152     hitsTot.start()
153     if task.return_flag(flags, "hitsSciFi")==1:
154         hitsSciFi.start()
155     if task.return_flag(flags, "hitsUS")==1:
156         hitsUS.start()
157     if task.return_flag(flags, "hitsDS")==1:
158         hitsDS.start()
159     if task.return_flag(flags, "hitsBM")==1:
160         hitsBM.start()
161
162     #vetoCh.start()
163     if task.return_flag(flags, "sciFiCh")==1:
164         sciFiCh.start()
165     if task.return_flag(flags, "usCh")==1:
166         usCh.start()
167     if task.return_flag(flags, "dsCh")==1:
168         dsCh.start()
169     if task.return_flag(flags, "bmCh")==1:
170         bmCh.start()
171
172     if task.return_flag(flags, "mapSciFi1")==1:
173         mapSciFi1.start()
174     if task.return_flag(flags, "valUS1")==1:
175         valUS1.start()
176     if task.return_flag(flags, "valUS2")==1:
177         valUS2.start()
178     if task.return_flag(flags, "valUS3")==1:
179         valUS3.start()
180     if task.return_flag(flags, "valUS4")==1:
181         valUS4.start()
182     if task.return_flag(flags, "valUS5")==1:
183         valUS5.start()
184     if task.return_flag(flags, "valDS1V")==1:
185         valDS1V.start()
186     if task.return_flag(flags, "valDS1L")==1:
187         valDS1L.start()
188     if task.return_flag(flags, "valDS1R")==1:
189         valDS1R.start()
190
191
192     # valScifi1x.start()
193     if task.return_flag(flags, "scatValUS1")==1:
194         scatValUS1.start()
195     if task.return_flag(flags, "scatValUS2")==1:
196         scatValUS2.start()
197     if task.return_flag(flags, "scatValUS3")==1:
198         scatValUS3.start()
199     if task.return_flag(flags, "scatValUS4")==1:
200         scatValUS4.start()
201     if task.return_flag(flags, "scatValUS5")==1:
202         scatValUS5.start()
203     if task.return_flag(flags, "scatValUS1R2R")==1:
204         scatValUS1R2R.start()
205     if task.return_flag(flags, "scatValUS1L2L")==1:
206         scatValUS1L2L.start()
207     if task.return_flag(flags, "scatValUS1R1V")==1:
208         scatValUS1R1V.start()
209
210     if task.return_flag(flags, "alignUS")==1:
211         alignUS.start()
212

```

```
213     if task.return_flag(flags, "planeUS")==1:
214         planeUS.start()
215     if task.return_flag(flags, "planeDS")==1:
216         planeDS.start()
217     if task.return_flag(flags, "planeSciFi")==1:
218         planeSciFi.start()
219
220     if "stable" in args.beammode:
221         lumi.start()
222
223     #rate should ALWAYS be running!
224     rate.start()
225     while(True):
226         if (ROOT.gSystem.ProcessEvents()):
227             break
```

Bibliography

- [1] G. Co'. "Neutrini ed interazione debole". In: *Ithaca: Viaggio nella Scienza VI*. 2015.
- [2] C. L. Cowan et al. "Detection of the Free Neutrino: a Confirmation". In: *Science* 124.3212 (1956), pp. 103–104. DOI: 10.1126/science.124.3212.103. eprint: <https://www.science.org/doi/pdf/10.1126/science.124.3212.103>. URL: <https://www.science.org/doi/abs/10.1126/science.124.3212.103>.
- [3] F. Reines and C. Cowan. "The Reines-Cowan experiments: Detecting the Poltergeist". In: *Los Alamos Sci.* (1997).
- [4] Carlo Giunti and Chung W. Kim. *Fundamentals of Neutrino Physics and Astrophysics*. Oxford University Press, 2007. DOI: 10.1093/acprof:oso/9780198508717.001.0001. URL: <https://doi.org/10.1093/acprof:oso/9780198508717.001.0001>.
- [5] J. A. Formaggio and G. P. Zeller. "From eV to EeV: Neutrino cross sections across energy scales". In: *Reviews of Modern Physics* (2012). DOI: 10.1103/revmodphys.84.1307. URL: <https://doi.org/10.1103/revmodphys.84.1307>.
- [6] Michael E. Peskin. "The Current-Current Model of the Weak Interaction". In: *Concepts of Elementary Particle Physics*. Oxford University Press, 2019. ISBN: 9780198812180.
- [7] Y. Nakajima et al. "Measurement of inclusive charged current interactions on carbon in a few-GeV neutrino beam". In: *Physical Review D* (2011).
- [8] Janet M. Conrad, Michael H. Shaevitz, and Tim Bolton. "Precision measurements with high-energy neutrino beams". In: *Reviews of Modern Physics* (1998).
- [9] LHC Collaboration. *SND@LHC: The Scattering and Neutrino Detector at the LHC*. 2023. arXiv: 2210.02784 [hep-ex].
- [10] Mauricio Bustamante and Amy Connolly. "Extracting the Energy-Dependent Neutrino-Nucleon Cross Section above 10 TeV Using IceCube Showers". In: *Phys. Rev. Lett.* (2019). DOI: 10.1103/PhysRevLett.122.041101. URL: <https://link.aps.org/doi/10.1103/PhysRevLett.122.041101>.

- [11] Sheldon L. Glashow. “Resonant Scattering of Antineutrinos”. In: *Phys. Rev.* (1960).
- [12] E.Kh. Akhmedov, G.C. Branco, and M.N. Rebelo. “Seesaw mechanism and structure of neutrino mass matrix”. In: *Physics Letters B* (2000). DOI: 10.1016/s0370-2693(00)00282-3. URL: <https://doi.org/10.1016%2Fs0370-2693%2800%2900282-3>.
- [13] Salvatore Mele. “The Measurement of the Number of Light Neutrino Species at LEP”. In: *Adv. Ser. Dir. High Energy Phys.* (2015). DOI: 10.1142/9789814644150_0004. URL: <http://cds.cern.ch/record/2103251>.
- [14] Andreas Aste. “Weyl, Majorana and Dirac Fields from a Unified Perspective”. In: *Symmetry* 8.9 (Aug. 2016), p. 87. DOI: 10.3390/sym8090087. URL: <https://doi.org/10.3390%2Fsym8090087>.
- [15] Robert Foot et al. “Seesaw Neutrino Masses Induced by a Triplet of Leptons”. In: (1989). DOI: 10.1007/BF01415558.
- [16] Asli M Abdullahi et al. “The present and future status of heavy neutral leptons”. In: *Journal of Physics G: Nuclear and Particle Physics* (2023). DOI: 10.1088/1361-6471/ac98f9. URL: <https://doi.org/10.1088%2F1361-6471%2Fac98f9>.
- [17] Takehiko Asaka and Mikhail Shaposhnikov. “The ν MSM, dark matter and baryon asymmetry of the universe”. In: *Physics Letters B* (2005). DOI: 10.1016/j.physletb.2005.06.020. URL: <https://doi.org/10.1016%2Fj.physletb.2005.06.020>.
- [18] Alexey Boyarsky et al. “Searches for new physics at SND@LHC”. In: *Journal of High Energy Physics* 2022.3 (Mar. 2022). DOI: 10.1007/jhep03(2022)006. URL: <https://doi.org/10.1007%2Fjhep03%282022%29006>.
- [19] Ubaldo Dore and Lucia Zanello. *Bruno Pontecorvo and neutrino physics*. 2010. arXiv: 0910.1657 [physics.hist-ph].
- [20] Giovanni De Lellis, Pasquale Migliozi, and Pietro Santorelli. “Charm physics with neutrinos”. In: *Phys. Rept.* (2004). DOI: 10.1016/j.physrep.2005.02.001.
- [21] Tanju Gleisberg et al. “SHERPA 1.alpha, a proof-of-concept version”. In: *Journal of High Energy Physics* (2004). DOI: 10.1088/1126-6708/2004/02/056. URL: <https://dx.doi.org/10.1088/1126-6708/2004/02/056>.
- [22] Alexey Boyarsky et al. “Searches for new physics at SND@LHC”. In: *Journal of High Energy Physics* 2022 (2022). DOI: 10.1007/jhep03(2022)006. URL: <https://doi.org/10.1007%2Fjhep03%282022%29006>.
- [23] R. Albanese et al. “Observation of Collider Muon Neutrinos with the SND@LHC Experiment”. In: *Phys. Rev. Lett.* (2023). DOI: 10.1103/PhysRevLett.131.031802. URL: <https://link.aps.org/doi/10.1103/PhysRevLett.131.031802>.

- [24] N Beni et al. “Physics potential of an experiment using LHC neutrinos”. In: *Journal of Physics G: Nuclear and Particle Physics* (2019). DOI: 10.1088/1361-6471/ab3f7c. URL: <https://dx.doi.org/10.1088/1361-6471/ab3f7c>.
- [25] C Ahdida et al. *SND@LHC - Scattering and Neutrino Detector at the LHC*. Tech. rep. CERN, 2021. URL: <http://cds.cern.ch/record/2750060>.
- [26] *PYTHIA 8*. <https://pythia.org/>.
- [27] Simona Ilieva Ilieva. “Measurement of the muon flux at SND@LHC”. In: (2023). URL: <http://cds.cern.ch/record/2859193>.
- [28] *PyDIM*. <https://dim.web.cern.ch/PyDIM/doc/api/html/index.html>.
- [29] *TOFPET 2C/D SiPM readout ASICS*. PETsys Electronics. 2017.
- [30] *sndsw*. <https://github.com/SND-LHC/sndsw>.
- [31] *Real Time Data Quality Monitor for SND@LHC*. https://github.com/FelixofRivia/SNDatLHC_RTDM.

Acknowledgements

As I come to the end of this thesis, I would like to take a page to thank those who have supported me, directly or indirectly, during this journey.

I would like to thank Prof. Maurizio Spurio and Dr. Marco Dallavalle for all the provided opportunities, advice and help in writing this thesis. In particular for the inclusion in the SND@LHC research group.

I would like to thank Federico for his patience, valuable teachings and constant software support.

I would like to thank Giulia for always encouraging me, listening to me, and helping me with all kinds of tasks.

I am truly grateful to the SND@LHC collaboration members for their helpfulness and friendliness.

Many thanks go to my family, who have always believed in my abilities.

Finally, I would like to thank all my friends for their encouragement and support.